This manuscript is a preprint and has been formally accepted for publication in **Basin Research.**

EXTENSIONAL DEFORMATION OF A SHALE-DOMINATED DELTA: TARAKAN BASIN, OFFSHORE INDONESIA

Aurio Erdi[1,2], Christopher A-L. Jackson[1,3], Juan I. Soto[4,#]

[1]Basin Research Group (BRG), Department of Earth Science and Engineering, Imperial College, London, United Kingdom

[2]Research Centre for Geological Resources, National Research and Innovation Agency (BRIN), Indonesia

[3]Jacobs, Manchester, United Kingdom

[4]Bureau of Economic Geology, Jackson School of Geosciences, The University of Texas at Austin, University Station, Box X, Austin, Texas, 78713-8924, USA

[#]On leave of absence from: Departamento de Geodinámica, Universidad de Granada, Avenida de Fuente Nueva s/n, 18071 Granada, Spain

Corresponding author:

Aurio Erdi, Basin Research Group (BRG), Department of Earth Science and Engineering, Imperial College, Prince Consort Road, London, S W7 2BP, United Kingdom.

Email: a.erdi18@imperial.ac.uk/auri002@brin.go.id

Abstract

Deformation on shale-rich continental margins is commonly associated with thin-skinned extension above mobile shales. Normal faulting and shale mobilization are widespread on such margins, being associated with and controlled by progradation and gravitational failure of deltaic sedimentary wedges. However, due to uncertainties in seismically imaging mobile shales, our understanding of problems like how base mobile-shale controls deformation, and the shape, size, and distribution of shale structures remain poorly understood. We here use 3D seismic reflection data from the platform region of the Tarakan Basin, offshore eastern Indonesia to investigate the temporal and spatial evolution of thin-skinned deformation of the Neogene sedimentary section. Our detailed seismic interpretation reveals up to 74 km long, concave- and convex-into-the-basin normal faults, dipping both basinward (eastwards) and locally landward (westwards), which detach downwards on a basal mobile shale (Early-Middle Miocene). The base of the mobile shale unit dips gently (< 17^{o}) seaward, although older (Eocene-Early Miocene), rift-related normal faults originate local structural highs deforming the base of mobile shales. Our isochore (thickness map) analysis shows that supra-shale normal faulting commenced in the Middle Miocene and was accompanied by the formation of hanging-wall rollover folds and associated crestal grabens, with the subsequent along- and across strike migration of the deformation related to the nucleation, lateral linkage, and reactivation of individual fault systems. Updip growth normal faulting was also accompanied by the downslope flow of mobile shale, accompanied by parallel and perpendicular variations of the differential loading in the delta system, and local contraction and mobile shale-upbuilding, resulting in the growth of large, margin-parallel shale anticlines further downdip. The growth faults and anticlines are locally overlain by up to 5 km tall of mud pipes and volcanoes. We suggest that variations in the rate of sedimentary loading, mobile shale flow, fault growth, and gravitational failure of the delta system above a seaward-dipping, but locally rugose base mobile-shale surface, controlled Neogene deformation in the Tarakan Basin. We also demonstrate how variations in the trend and dip of the base mobile-shale surface influences the position, timing of formation, and evolution of supra-shale normal faults and their associated depocenters along shale-rich, deltaic margins.

Keywords:

shale tectonics; base mobile-shale surface; deltaic continental margin; gravity driven deformation; mobile shale flow; normal faulting

Highlight:

- Neogene deformation in the Tarakan Basin are shown by growth normal faults, shale rollers and anticlines, and mud pipes and volcanoes.
- Mobile shale flow across vary dipping of base mobile-shale surface, gravitational loading and gliding, controlled the deformation.
- The growth faults grew by tip propagation and segment linkage, and late-stage tip retreat and reactivation.
- Dipping of base mobile-shale controls position, timing, and evolution of growth faults and their associated depocenters.

1. **Introduction**

Shale-rich, deltaic continental margins may be characterized by thin-skinned, gravity-driven deformation above an unconsolidated, overpressured, buried shale (e.g. Damuth, 1994; Morley and Guerin, 1996; Cohen and McClay, 1996; Briggs et al., 2006; Espurt et al., 2009; Morley et al., 2011; Santos Betancor and Soto, 2012; Rowan, 2020; Zhang et al., 2021). However, difficulties with seismically imaging mobilized shale bodies mean that we have a poor understanding of the shape and size of these bodies, and of their mechanisms (e.g., brittle vs. ductile) and involved deformation (see Hudec and Soto, 2021 and Soto et al., 2021a). For example, Van Rensbergen and Morley (2000; 2003) use 2D seismic data to document chaotic seismic facies, being interpreted to reflect thick, mobile shale in footwall of shale-detached listric normal faults. However, in higher quality data imaging the same profile, they could interpret a structurally much simpler, fault-related horst, with a large shale body being absent. Their study illustrates how improvements in subsurface imaging can provide a better understanding of the structural style and kinematic evolution of shale tectonics along deltaic continental margins.

In the proximal domain of deltaic continental margins, thin-skinned deformation is typically characterized by basinward- and landward-dipping listric growth faults and mud diapir and pipes (e.g. Damuth, 1994; Van Rensbergen et al., 1999; Morley, 2003a; Totterdell and Krassay, 2003; Espurt et al., 2009; Sapin et al., 2012; Rowan, 2020; Ahmed et al., 2022). Extensional deformation of the supra-shale overburden and the rise of diapiric shale are controlled by rapid progradation of sedimentary wedges and gravitational gliding (e.g. Evamy et al., 1978; Cohen and McClay, 1996; Morley, 2003a; Espurt et al., 2009). The ultimate structural style and evolution are influenced by differential compaction of the progradational succession (e.g. Van Rensbergen and Morley, 2000; Fazlikhani and Back, 2015a), the presence of pre-existing shale structures (e.g. Sapin et al., 2012; Fazlikhani and Back, 2015b), temporal and spatial variations in sediment accumulation rates (e.g. Rouby et al., 2011; Chima et al., 2022), the existence of fluid expulsion structures (Back and Morley, 2016), the variation of dips on base mobile-shale surfaces (Wu et al., 2015), the deep flow of mobile shale under either brittle or ductile conditions (e.g. Cohen and McClay, 1996; Soto et al., 2021a), and the growth history of supra-shale faults (e.g. Fazlikhani and Back, 2012). Most of studies listed above provide only two-dimensional treatments of shale tectonics and only very few have inspected their three-dimensional evolutions (Van Rensbergen and Morley, 2003; Fazlikhani and Back., 2012, 2015b; Santos Betancor and Soto, 2012; Ahmed et al., 2022).

The Tarakan Basin, offshore Indonesia is an example of a deltaic continental margin containing thick, mobile shale (Fig. 1). The basin is separated from the onshore region by thick-skinned normal faults (MRNF; e.g. Hidayati et al., 2007). The offshore area is characterized by shale-detached (i.e., thin-skinned), NE-SW-striking, basinward- and landward-dipping extensional (e.g. Heriyanto et al., 1992, Lentini and Darman, 1996) or inverted (e.g. Biantoro et al., 1996; Maulin et al., 2021) growth faults, and several NW-trending folds, which have been traditionally called arches (e.g. Wight et al., 1993) (Fig. 1). The kinematics and origin of the growth faults and folds are debated, falling into two end-member models: (i) a strike-slip faulting (e.g. Wight et al., 1993; Lentini and Darman, 1996; Hidayati et al., 2007); and (ii) an uplift of pre-existing rift-related topography (e.g. Sapiie et al., 2021). However, these previous studies use two-dimensional seismic reflection data that have relatively poor imaging of deeper part of the basin, including the interval containing mobile Neogene shale. Thus, a study based on high-quality, preferably 3D seismic reflection data is needed to test these models and to underpin a detailed reconstruction of the structural style and evolution of the basin.

We here use high-quality, 3D seismic reflection datasets imaging the shelf-edge to upper-slope of the Tarakan Basin to answer the following two key questions: (i) how does Neogene extensional deformation in this relatively proximal part of the Tarakan Basin relate to the broader tectonic and geodynamic setting of the region?; and, (ii) what are the spatial and kinematic relationships between sub- and supra-shale deformation in the proximal, extension-dominated domain of a shale-dominated delta. We identify a deltaic sedimentary wedge that prograde seaward into the Tarakan Basin above mobile shale that overlay several N-to-NE-trending, base mobile-shale highs. The delta wedge, including its underlying mobile shale, is deformed by arrays of NNE-SSW-striking, shale-detached, basinward- and landward-dipping growth fault systems and shale structures (i.e. shale rollers, anticlines, mud pipes, and mud volcanoes). Using seismic-stratigraphic and isochore analysis, we reconstruct six main stages in the post-Eocene structural evolution of the basin.

2. **Geological Setting**

The Tarakan Basin is located offshore NE Borneo Island, within Indonesia territory (Achmad and Samuel, 1984). The basin is located in a structurally complex zone of continental convergence involving subduction of Northern Sulawesi (e.g. Hall, 2013; 2019; Watkinson and Hall, 2017) (Fig. 1a). The western, yet still offshore part of the basin is thought to be separated from the eastern part of the onshore region by a large, thick-skinned normal fault (e.g. Hidayati et al., 2007). The Tarakan Basin stretches eastwards into Celebes Sea (Fig. 1a). To the north and south, the basin is bounded by the Sampoerna and Mangkalihat strike-slip fault zones, respectively (e.g. Lentini and Darman, 1996).

Borneo Island and adjacent areas were subject to three main stages of Paleogene lithospheric deformation (Fig. 2): (i) a counter-clockwise rotation of Borneo of ca. 35^{o} in Late Eocene (41.2–33.9 Ma) (Advokaat et al., 2018) ; (ii) onset of rifting in Makassar Strait in Middle-Late Eocene (38-36 Ma) until Early Miocene (Situmorang, 1982; Satyana, 2015), which possibly simultaneous with the opening of the Celebes Sea (Lentini and Darman, 1996) and/or the generation of the Tarakan Basin (Satyana et al, 1999; Krisnabudhi et al., 2021).

Variations of the location and magnitude of lithospheric deformation and sedimentation occurred in the Borneo and adjacent areas since Early Neogene. The lithospheric deformation were reflected by: (i) an additional counter-clockwise rotation of 10^{o} occurred since Early Miocene (23 Ma) (Advokaat et al., 2018), possibly being related to Banda Arc subduction (e.g. Spakman and Hall, 2010); and, (ii) a progressive, Borneo uplift that was related to Sabah orogeny of Hutchison (1996) since the latest Early Miocene (17 Ma) (Lunt and Madon, 2017); (iii) rifting cessation and thermal subsidence of Makassar strait (Situmorang, 1982; Satyana, 2015). The interaction of uplift and subsidence events since Neogene resulted in originating: (i) onset of rapid sedimentation of up to 10 km thick deltaic sequence (Hall and Nichols, 2002; Lunt and Madon, 2017; Lunt, 2019) that unconformably overlay Oligocene sedimentary unit in NW and N Borneo (SEAU 52 in Fig. 2; e.g. Brondijk, 1962; Balaguru, 2008; Balaguru et al., 2003; Lunt and Madon, 2017; Morley et al., 2021; Krisnabudhi et al., 2022); (ii) associated gravity-driven deformation around offshore Borneo, such as West Luconia, Baram and Tarakan delta (e.g. Morley, 2003a; Morley et al., 2011); and, (iii) several regional, Neogene unconformities that span the South China sea and NW Borneo (e.g. Levell, 1987; Hutchison, 2005; Cullen, 2010, 2014; Madon et al., 2013; Lunt and Madon, 2017; Krisnabudhi et al., 2022).

The thick deltaic sequences in NW and NE Borneo contain an Early Miocene , kaolinite- and illite-rich shale unit (Morley, 2003a), which is called Setap shale (e.g. Brondijk, 1962; Balaguru et al., 2003; Lunt and Madon, 2017; Jamaludin et al., 2021) and Tarakan mobile shale unit (e.g. Putra et al., 2017; Maulin et al., 2021). More specifically, in the Tarakan Basin, rapid sedimentation of this deltaic sequence began up to 17.3 Ma (Noon et al., 2003; Morley et al., 2017; Krisnabudhi et al., 2022), and was associated with a marked increase in sediment accumulation rates (from 60 to 160 m/my) (Fig. 2; Hidayati et al., 2007).

During the Middle-Late Miocene, the tectono-stratigraphic development of the Tarakan Basin and surrounding areas was controlled by lithosphere-scale (i.e., thick-skinned) and/or gravity-driven (i.e., thin-skinned) deformation. On the shelf edge of the Tarakan Basin, listric growth faults formed (e.g. Wight et al., 1993; Lentini and Darman, 1996), detaching downward along the Early-Middle Miocene sequences (e.g. Hidayati et al., 2007; Putra et al., 2017; Sapiie et al., 2021; Maulin et al., 2021; Krisnabudhi et al., 2022). There are also deeper, rift-related normal faults affecting the basement- (Biantoro et al., 1996; Krisnabudhi et al., 2022). Middle-Late Miocene deformation was coeval with a progressively increasing rate of sediment accumulations (from 160 to 330 m/my) and a global sea-level fall after the Middle Miocene climatic optimum (MMCO) (SEA59; Fig. 2) (Hidayati et al., 2007; Morley et al., 2021). In northern Borneo, although there was a pause in 12-13 Ma, the uplift broadly continued, being related to the Sabah orogeny (Lunt and Madon, 2017), deep crustal flow in respond to sedimentary loading (Morley and Westway, 2006), and originating the simultaneous Kinabalu magmatism (Hall, 2013). This uplift was accompanied by the rapid subsidence and the sedimentary accumulation of 15 km in offshore Borneo (Graves and Swauger, 1997), forming the Central Basin of eastern Sabah (see inset of Fig. 1a) (Hall, 2013; Lunt and Madon, 2017).

Since the Pliocene, the shelf edge of the Tarakan Basin was subject to both folding and reverse faulting (Fig. 1a). Two alternative models haven been proposed to explain their origins: (i) wrenching along the Maratua and Sampoerna strike-slip faults (Wight et al., 1993; Lentini and Darman, 1996; Hidayati et al., 2007), or; (ii) distal uplift of the deeper faults (Sapiie et al., 2021). These models resulted in inversion of formerly extensional listric normal faults, and the formation of NW-trending arches around the shelf edge and upper slope of Tarakan Basin (e.g. Wight et al., 1993; Lentini and Darman, 1996; Hidayati et al., 2007, Maulin et al., 2021). Regardless of their origin, formation of these structures occurred during the Pliocene-Recent (e.g. Lentini and Darman, 1996), a period characterised by a high sedimentation rate, which was as high as 820 m/my in shelf areas (Fig. 2). In contrast, in the distal areas of the basin the sedimentation rate was <330 m/my, because much of the Plio-Pleistocene sediment supply was trapped on the shelf (Hidayati et al., 2007).

We focus on the shelf-edge to upper slope of the Tarakan Basin, where at least five different onshore-river systems supplied sediment to the offshore basin (Fig. 1). Wells in this proximal area reveal also overpressure conditions within the Middle-Late Miocene sequences (Putra et al., 2017; Maulin et al., 2019). Previous studies identified that the shelf-edge contains a range of basinward- and landward-dipping extensional and/or inverted growth faults, and is situated at the southern tip of the Bunyu Arch (e.g. Wight et al., 1993; Lentini and Darman, 1996; Hidayati et al., 2007; Maulin et al., 2021; Sapiie et al., 2021).

3. **Datasets and Methods**

We focused on an area imaged by two 3-D Kirchhoff pre-stack time migration (PSTM) seismic reflection datasets (TBN-10 in the north and TBB-11 in the south; Table 1). These two datasets overlap by ~70 km^2, and have similar inline and cross line spacings of 25 m (see complete details of the seismic datasets in Table 1). Inlines (NE and N) and crosslines (NW and W) trend broadly normal and parallel to the bulk SE tectonic translation direction of the supra-shale cover, respectively. The seismic data are displayed with the Society of Exploration Geophysics (SEG) reverse polarity, whereby a downward increase and decrease in acoustic impedance are represented by a negative and positive reflection events, respectively.

Kirchhoff PSTM data has some disadvantages when attempting to image structurally and stratigraphically complex areas. For example, such data might contain fault shadows, and they may not image shale structures as well as other seismic reflection data types (e.g. Fagin, 1996; Elsley and Tieman, 2010; Soto et al., 2021b). Still, our PSTM data are of sufficient quality to distinguish the main shale and supra-shale structures (Tables 2-4; see also table S1-S2). These data are in time, therefore the height of shale structures and/or the calculation of dip on base mobile-shale surface, for example, are converted from two-way time (TWT) to kilometres using seismic velocity data (e.g. Johnson and Hansen, 1987), ranging from 3500 m/s at seismic horizon H1 to 1500 m/s at seabed (Table 2).

The seismic data were provided by TGS and are commercially sensitive. As such, we cannot provide the precise geographic location of seismic profiles (although the dataset is located along a delta-fed part of NE Borneo; Fig. 1) or the specific locations of wells on the profiles. NW-to-W-trending seismic profiles (i.e., crosslines) normal to the broadly north-easterly margin trend are displayed from north to south (Figs 3 and 4; see also appendix S1 for uninterpreted profiles), and these accompanied by a margin-parallel profile trending north-east (Fig. 5). In the profiles, we also include an estimate of the dip of the base mobile-shale surface (Figs 3-5). However, given that the profiles are in time, dips are approximate and relative values.

We map eight key seismic horizons (H1, TMB, H2-7) by identifying distinctive reflections and their terminations (i.e. onlap, toplap, and unconformities; Mitchum et al., 1977) (Table 2 and Fig. 6). The critical top mobile shale (TMB) is not constrained by well data, given no wells drill that deeply in the Tarakan Basin. As such, we infer the presence of deep shale using the seismic-reflection criteria established by previous shale tectonic studies (Table 2). The ages of other key horizons are established by integrating: (i) the regional tectonic events affecting Borneo since the Oligocene; and (ii) published data from the Vanda-1 well (Netherwood and Wight, 1992; Wight et al., 1993) (Figs 1-2). These show that H1 is Lower Miocene(?) (using age of regional unconformities identified in Borneo; i.e., DRU of Levell, 1987; SCSU of Cullen, 2010, 2014; EMU of Madon et al., 2013; SEA52U of Morley et al., 2021), whereas TMB and H2-H3 are early Middle-Upper Miocene(?). The age of younger seismic horizons (i.e., H4-H7; uppermost Miocene to Upper Pleistocene) are directly constrained by the Vanda-1 well.

We use our seismic interpretations to generate isochore (i.e. vertical thickness) maps for the mobile shale and six overburden units. We realized that the base mobile-shale (H1) locally extends below the depth imaged by our seismic data (> 8.0 s TWT or 14 km in TBN-10; Table 1), resulting in an underestimation of mobile shale thickness in this area (Fig. 7). However, our data and derived maps clearly reveal the main shale structures present within the basin. Because of: (i) limitations of seismic velocity data to undertake a regionally consistent depth conversion (e.g. Johnson and Hansen, 1987; Francis, 2018); and (ii) our primary interest being in the relative rather than absolute changes of fault length along strike (cf. Fazlikhani and Back, 2012), we present the structure and isochore map in time (ms TWT), rather than depth (Figs 8-9). Along strike change of fault throw for supra-shale faults, however, are qualitatively illustrated by change of size of fault surface in maps (Figs 8-9).

4. **Base mobile-shale structural style**

The base mobile-shale (H1) is, although locally speculative near the bottom edge of dataset, can be defined by a continuous, weak, positive reflection, located immediately above the upper tips of sub-shale faults and below chaotic weak-to-moderate reflections (Figs 3-5; Table 2). These faults are apparently planar, and dip speculatively steep (~70^{o}) basinward- and landward. The largest throw on these faults (≤ 1 s TWT or 1 km) is observed in the southwestern and southern area that cut the H1 (Fig. 4b). The lower tips of these faults are below the depth imaged by these seismic data (Table 1).

The base mobile-shale dips gently basinwards (1-17^{o}); i.e., SE (Figs 3-5). This surface is broadly convex-upward, being characterized by a large structural low in the centre of the study area, and, in the north and south, local, N-to-NE-trending structural-highs (ca. 1.5 s TWT or up to 2 km high; labelled “SH” of Figs 3-5, 7b). These highs is broadly coincided to long (< 27 km), NNE-

SSW-striking normal faults (Fig. 7b). Most of these faults dip basinwards, although some segments, which are more abundant in the south, dip landward.

5. **Shale Structures**

The top-mobile shale horizon is defined by a strong, negative reflection (TMB; Figs 3-5 and 6a-b). Given that the presence of methane in undercompacted shales can produced a strong, negative reflection (e.g. Soto et al., 2021b), we speculate that the negative reflection observed here defines the contact between normally compacted shales and overlying, methane-rich (possibly undercompacted) mobile shales. The seismic sequence below the TMB reflection contains various diffractions and noise, although we locally observe continuous, weak-to-moderate amplitude reflections (label "x"; Figs. 4-5 and 6a). Internal reflections similar to these have been observed in other shale regions, for example the Gulf of Mexico, being interpreted either as a pre-existing, now-deformed stratigraphic fabrics, or a new deformation fabric formed by the flow of mobile shales under critical-state conditions (Soto et al., 2021b).

Mobile shale thickness map (< 2.75 s TWT or 3.5 km thick) shows how thickness of this unit *presently* varies across the study area, being thickest in the centre and east, thinning northward and southward (Fig. 7c). The thickest mobile shale coincides with the structural low seen on the base mobile shale map in the centre of the area, whereas the thinner areas coincide with the base mobile-shale structural-highs identified in the north and south (cf. Figs 7a-b and 7c).

5.1 Shale rollers

These structures are defined by broadly asymmetrical, triangular zones of mobile shale that have a pointed crest and are flanked on one side by basinward-dipping, shale-detached normal faults (label SR; Table 3 and Figs 3-5, 6a, 7c). These structures are interpreted as shale rollers, with their geometry and relationship to normal faults suggesting they formed via reactive diapirism during thin-skinned extension (e.g. Morley and Guerin, 1996; Hudec and Soto, 2021). They are thus comparable to salt rollers formed in salt basins (e.g. Brun and Mauduit, 2009;

Jackson and Hudec, 2017). Shale rollers are broadly distributed across the study area, typically trending N-to-NE, sub-parallel to the sub-shale normal faults (cf. Figs 7a-b and 7c).

5.2 Shale anticlines

These structures are characterised by broadly symmetric, low-amplitude, long-wavelength anticlines, and with a single, angular-to-rounded hinge line (label SA; Figs 4b, 6b and 7c). They usually verge basinward (i.e. SE), with a sub-horizontal eastern limb and a more steeply-dipping western limb (≤ 55^{o} dip). These structures are restricted to the distal, eastern part of the study area, and their axes trend parallel to the shale rollers (i.e. N-NE; Fig. 7c).

5.3 Mud pipes

Mud pipes (s. Kopf, 2002) are defined by cylindrical domains with some isolated, low-amplitude, very low reflectivity of some isolated, sub-vertical, chaotic reflections (label MP; Table 3, Figs 4b and 6c). The external boundaries of these structures are sub-vertical, crosscutting the adjacent, layered sequences that loss progressively their reflectivity towards the pipe (label "iii" in MP; Table 3). Mud pipes occurs as deep as the H2 reflection, with their shallower heads deforming sequences near the H4 reflection (label MP; Table 3, Figs 4b and 6c).

The upper parts of some of the mud pipes are characterised by a broad (up to 4.3 km wide), tear drop-shaped area of low reflectivity, which may contain isolated, internal reflections (MP; Fig. 4b). These reflections may reflect remnant fragments of the host rock, imbedded within the ascending diapiric material, which itself is poorly reflective. The lower part of the mud pipes is more difficult to identify, and is commonly defined by a narrow, sub-vertical domain with crosscutting reflections that connect with the crest of deeper, shale-cored anticlines (label "i" in MP; Table 3). The mud pipe seen in the distal area affects H2-H4, defining an elongated structure parallel to the underlaying shale anticlines (Fig. 8a-b).

The seismic characteristics of the mud pipes, their cylindrical 3D geometry, their position at the anticline crests, as well as the nature of their contacts with the host rock suggest the existence of pervasive fluid migration from the mobilized, overpressured muds along these conduits piercing the country sediments (e.g. Kopf, 2002; Santos Betancor and Soto, 2015).

5.4 Mud volcanoes

These structures are defined by conical mounds (e.g. Kopf, 2002) that are identified as deep as the H4 reflection structural level, and which can affect younger sequences up to the seabed (Fig. 3b; Table 3). The deeper domains of mud volcanoes, i.e., below H4, are accompanied by chaotic reflections that are seen on the hanging-wall of normal faults (F6; Fig. 3b). At the shallower level, near H7, they form elliptical edifices parallel to the deeper and adjacent normal faults (Figs 8c-d). Given their vertical distributions, we suggest that mud volcanoes are formed by injection of fluidized material along hydro-fractures (e.g. Morley, 2003a; Hudec and Soto, 2021).

6. **Supra-shale Structures**

The supra-shale structural framework is characterized by two main types of structures (Table 4; Figs 3-6). The first type is defined by major basinward (F1-F16)- and landward (C1-C9)-dipping listric faults that die-out downward into the mobile shales and which tip-out upward between H4 and the seabed. The basinward-dipping listric faults detach downward onto the flanks of shale rollers and are flanked by hanging-wall growth strata (Figs 3-6). These faults are common on the shelf margin-to-upper slope (Fig. 1b), suggesting they formed in response to overburden extension due to gravitational failure of the deltaic wedge within which they developed (e.g. Morley, 2003a; Soto et al., 2010; Hudec and Soto, 2021), and/or extension driven by differential compaction and fluid expulsion (e.g. Van Rensbergen and Morley, 2000; 2003; Back and Morley, 2016). Similar to the basinward-dipping, the landward-dipping listric faults in the south are flanked by hanging-wall growth strata. However, these hanging-wall-related growth strata show progressively younger basinward, suggesting they formed in response to sedimentary loading during delta progradation (Fig. 4) (e.g. Morley and Guerin, 1996; Ge et al., 1997; McClay et al., 2003; Sapin et al., 2012). The basinward- and landward-dipping listric faults are associated with synthetic and antithetic normal faults that formed within the damage zones of the larger faults (e.g. McGrath and Davison, 1996), or that developed to accommodate locally high stresses occurring within relay zones between the major growth faults (Imber et al., 2003) (e.g. F7; Fig. 3b or C1-C3 and C6-C9; Fig. 4d). These faults have maximum displacement of up to 2.86 km on H2-H4 (Table 5), indicating their time of nucleation.

The second type of supra-shale structure is defined by NE-trending folds that are best-developed between H2 and H7, flanking the basinward- and landward-dipping listric normal faults (e.g., F1 in the north, and C3-C5 and C8-C9 in the south; Figs 3c, 4 and 9b-c, h-i; Table 4). Given their relationship to shale-detached faults, we interpret them as hanging-wall rollover folds (e.g. Dula, 1991; Imber et al., 2003; Brun and Mauduit, 2008). We observe these NE-trending roller folds and their associated listric faults, rather than NW-trending isoclinal fold, in the southern tip of Bunyu Arch (e.g. Wight et al., 1993; Lentini and Darman, 1996), a NW-trending roller fold (F1, F7 and F9; Figs 3c and 8-9). Above the crests of roller folds, we observe symmetrical grabens bounded by basinward- and landward-planar normal faults that either physically link with the deeper major faults with which the folds are associated, or detach downward within the overburden. For example, on the hanging-wall of C3-C4, several basinward- and landward-dipping normal fault arrays form a symmetrical graben (Fig. 4b-d). Based on their location above the fold crest, we infer that these minor normal faults reflect crestal extension and faulting in response of outer-arc bending of strata (e.g. McClay, 1990; Dula, 1991; Morley, 2007; Erdi and Jackson, 2021).

H2, H4 and H7 illustrate the geometry of the various supra-shale normal faults (Fig. 8). Basinward-dipping normal faults occur across the study area, whereas the landward-dipping normal faults are restricted to the south. Some fault segments are separated by NNE- or SSW-dipping, largely undeformed relay zones, such as C5 and C9 in the southeast (label RZ; Fig. 8). Many faults show broadly convex- and concave-landward geometries, such as F7-F12. More specifically, throw on the basinward-dipping normal faults broadly decreases southward (Table 5; Fig. 8).

7. **Temporal evolution of supra-shale deformation**

Having described the various shale structures and supra-shale structural styles, we now explore how these structures evolved in the shelf-edge to upper slope of the Tarakan Basin. We interpret the evolution based on observations from maximum displacement of faults (Table 5), and time-structure and isochore maps (Figs 7-9; see also S2 for a larger version). Isochore maps show temporal changes in sediment thickness, which we infer record changes in accommodation driven by the migration of deformation (Fig. 9a-f) (e.g. Wu et al., 2015; Erdi and Jackson, 2021).

7.1 Base mobile-shale detachment (Eocene-Early Miocene?)

The base mobile-shale is an unconformity that detaches sub-shale faults from the overlying mobile shale unit. Base mobile-shale surface is inferred to represent the 17 Ma unconformity that separates syn-rift from post-rift successions in the South China, Sulu seas (e.g. Madon et al., 2013; Cullen, 2010, 2014; Morley et al., 2021) and rifting cessation in Makassar strait (Situmorang, 1981; Satyana, 2015).Given that the geometries of the sub-shale faults (e.g., planar, basement-involved) are broadly consistent with the geometry of syn-rift faults in the regions (e.g. Schlüter et al., 1996; Nur' Aini et al., 2005; Franke et al., 2008), we speculate that sub-shale extensional faults are related to (i) the Eocene-Early Miocene(?), thick-skinned (i.e., lithosphere-involved) extensional event; (ii) a c. 45^{o} of anticlockwise, post-Eocene rotation of the Borneo Island (Advokaat et al., 2018). Although a component of oblique-slip cannot be ruled out, we speculate that this faulting was dominated by dip-slip movements. The general seaward dip of the base mobile-shale surface above these faults (Figs 3-4) likely reflects post-Miocene tectonic uplift of northern Borneo and its immediately offshore region (Fig. 2) (e.g. Hall., 2013).

7.2 Deposition and origin of the mobile shale unit (Early Miocene-early Middle Miocene?)

Tectonic of Borneo and surrounding area suggest deposition and origin of mobile shale in Tarakan during Early Miocene. At ca. 17 Ma, onset rapid sedimentation of clay-rich deltaic sequence occurred in Tarakan (e.g. Noon et al., 2003; Hidayati et al. 2007; Sudarmono et al., 2017; Morley et al., 2017), including mobile shale unit in Tarakan (Putra et al., 2017; Maulin et al., 2021) (Fig. 2). We suggest this unit deposited above the base mobile-shale unconformity (Figs 3-5). Several studies suggest that North Borneo underwent rapid uplift and erosion during this time due to the Sabah Orogeny (e.g. Hall and Nichols, 2002; Hall, 2013), providing fluvio-deltaic sediment in this area (van Hattum, 2013). As such, we infer the northern Borneo as a provenance area for the mobile shale unit in Tarakan.

Although we cannot conclusively resolve the exact nature of the processes mobilizing the shales, we speculate that combination of smectite-illite transformation, compaction, and increasing shear stresses by supra-shale normal faulting created overpressure conditions in this shaly unit (e.g. Soto et al., 2021a; Li et al., 2022). This interpretation is supported by (i) predominantly composition of kaolinite and/or illite on mudstone intrusion (36-54% kaolinite and illite; Morley, 2003b) and weathering of parent rock across rivers sediments around N-to-NE Borneo (41-55% kaolinite, 47-77% illite, <5-18%; s. Liu et al., 2012); (ii) scarce available information in the offshore area show that the Neogene sediments are rich in kaolinite and illite (5-18%) (Abdullah et al., 2016); (ii) disequilibrium compaction of base-deltaic sequence in North Borneo (Tingay et al., 2009). Rapid sedimentation of this shaly unit likely lead to fluid entrapment, making it possible to achieve the critical-state conditions to permit essentially solid-state flow at relatively lower shear stresses.

7.3 Stratal unit 1 (early Middle Miocene?)

7.3.1 Description

SU1 was deposited immediately above the mobile shale and thickens across some supra-shale listric faults (F1, F8, F10-F16, C1-C3, and C6-C7; Figs 3c, 4-5 and 9a). We identify the following three key thickness patterns within SU1; (i) fault-controlled depocenters spanning the entire present-day trace length (e.g., F1, F14-F16 and C1 in the northwest and the southeast; Figs 9a and 10); (ii) fault-controlled depocenters only span a short portion of the present-day fault traces (e.g., F8, F11, F3, C2-C3 and C6-C7; Figs 9a and 10); and (iii) fault-controlled depocenters flank onto normal fault traces that are physical contact with each other (F10-F11; Fig. 9a). These indicate that the F1, F14-F15 and C1 reach their final length during deposition of the SU1, while others reach it relatively later.

7.3.2 Interpretation

SU1 records 1 Myr time span of the ~16 Myr post-rift history, indicating listric fault arrays began to grow during deposition of the SU1 (Figs. 9g, 10 and Table 5). Following a synoptic plot, which compare fault length on the SU1 with overlying thickness maps, the faults grew in two different ways, either by: (i) a synchronous increase in fault throw and length, with associated fault segment linkage (i.e. in cases where SU1 depocenters flank only a portion of the fault trace length; e.g. F10-F11, F13, C2-C3, and C6-C7) (e.g. Walsh and Watterson, 1988; Dawers et al., 1993; Cartwright et al., 1995; Mansfield and Cartwright, 1996); or (ii) rapidly attaining their near-final lengths via lateral tip propagation (i.e. in the cases where SU1 depocenters span the entire fault traces, e.g. F1 and F14-F16; e.g. Morley, 2002; Walsh et al., 2003) (Figs 9g and 10).

More generally, nucleation of the supra-shale listric faults indicate establishment and progradation of one or several deltaic systems during the first 2.4 Myr post-rift history of the Tarakan Basin (cf. Morley and Guerin, 1996; Sapin et al., 2012; Back and Morley, 2016) (Fig. 9g). This interpretation is consistent with an increasing sediment accumulation rate (i.e. from 60 to 160 m/my) in the onshore Tarakan Basin during Early-Middle Miocene (Hidayati et al., 2007), and with global events of sea-level falls related to the MMCO at SEA59 (Morley et al., 2021) (Fig. 2).

7.4 Stratal unit 2 (Middle-Upper Miocene?)

7.4.1 Description

Thickness patterns in the SU2 shows that fault-controlled depocenters broadly persisted adjacent to the F1, F8, F10-F16, C1-C3, and C6-C7 (Fig. 9b), although in detail we note that: (i) across fault-thickening now occurred along or at the lateral tips of the present day traces of the F2-F5, F7, F10-F12, southern portion of F13, F15 and C2-C3, and C5-C7 (Figs 4b-c and 9b); (ii) C5 cross-cut fault-related thickening on the upper tip of F15 (Fig. 4b-c); and (iii) the SU2 displays no thickness variation across the northeastern portion and southeastern of F1 and F16 respectively (Fig. 9b).

Along the normal fault array in the southeast, SU2 displays thickness variations toward the axis of the mud pipe (MP; Fig. 9b). This unit shows a wedge-shape geometry and thicken toward F16, while upturned, and truncated on intra-SU2 against the mud pipe flanks above the underlying limb of shale anticline (label E2; Figs 4b and 6b). We also note that mud pipe-related thickness variations in SU2 appear inversely related to thickness variations associated with the F15-F16 and the underlying mobile shale (Figs 4a-c and 9b). For example, across fault thickening of SU2 toward the F15 occurs above an area where the underlying mobile shale is thin, whereas thinning of SU2 toward the pipe flank occurs where the underlying mobile shale is thick (Fig. 4b-c).

7.4.2 Interpretation

SU2 records thin-skinned, gravity-driven deformation during the subsequent ca. 5.6 Myr post-rift history of the Tarakan Basin, recording the complex growth and death of the supra-shale fault array. First, some normal faults continue to grow via tip propagation, relay breaching, and segment linkage (F8, F10-F12, C1-C3, and C5-C7; Figs. 9h and 10). This interpretation is supported by the observation that depocenters are distributed along the established faults (Fig. 9b). Second, following comparison between thickness patterns of the SU2 and SU1, new normal faults nucleated (F2-F5, F7, C5; Fig. 9h and Table 5). Finally, some fault segments became inactive (F1, F15-F16; Figs 4b-c, 9h and 10). More specifically to the F15, this fault speculatively death due to grew of the younger fault of C5 (Fig. 4b-c).

The normal fault growth during the Middle-Upper Miocene was coeval with the onset of shale anticlines growth in the southeast (SA; Figs 4b and 9b). The local truncation (E2) above the fold limbs indicates that rates of fold-related uplift were even higher than the increasing and relatively high sediment accumulation rate (from 100 to 220 m/my; Fig. 2). Two possible mechanisms can explain the shale folding at this time: (a) downslope gliding of the mobile shale producing distal contraction (i.e. Van Bemmelen, 1947; Evamy et al., 1978; Ramberg, 1981; Wight, 1993; Totterdell and Krassay, 2003), (b) combination of margin-parallel and perpendicular differential loading, compaction, fluid expulsion and slip along normal faults (cf. Mourgues et al., 2009; Ings and Beaumont, 2010; Lacoste et al., 2012; Back and Morley, 2016). The first mechanism is supported by the orientation of fold axes being parallel to the shale rollers and their associated normal faults (Figs 7c and 9b), indicating the fold is related to distal contractional folds that are kinematically linked to up-dip extension (Figs 2 and 9h). The second mechanism is supported by the inverse relationship between thickness patterns in the mobile shale and SU2.

For example, SU2 thickens onto the F15-F16 where the mobile shale is relatively thin to adjacent area (Figs 4b-c, and cf. Figs 7c and 9b), suggesting the existence of syn-kinematic differential loading by normal faulting and shale-withdrawal that promoted mobile shale upbuilding at the core of the distal fold. This mechanism is also supported by fault-controlled depocenter on the SU2 that are distributed relatively basinward to that observed in underlying stratal unit (Fig. 9b), suggesting a basinward migration of the prograding wedge. This basinward progradation of the wedge might produce differential margin-perpendicular sedimentary loading and a basinward migration and evacuation of the mobile shale creating horizontal (tectonic) compaction and fluid expulsion (e.g. Van Rensbergen and Morley, 2000; Mourgues et al., 2009; Ings and Beaumont, 2010; Lacoste et al., 2012; Back and Morley, 2016). Still, given that the base mobile-shale horizon show a larger structural low in the centre domain (Fig. 7a-b), differential margin-parallel sedimentary loading could also occur, resulting in an additional northeast-southwest flow of the mobile shales to fill that trough.

7.5 Stratal unit 3 (Upper?-uppermost Miocene)

7.5.1 Description

There are several important observations regarding SU3. First, SU3 thickens (by up to 2.25 s TWT or 3 km) across many of the major normal faults (F3-F4, F6, F7a, c-e, F8-F11 and C1a-d, C2, C3a, c-d; Fig. 9c). Second, SU3 broadly thickens towards and has a wedge-shaped geometry in the hanging-wall of some listric faults, which are located relatively basinward of those active during deposition of SU2 (F6, southern portion of C3, C4 and C8-C9; Figs 4b-d, 5 and 9c). Third, SU3 also has a wedge-shaped geometry adjacent to and thickens towards the lateral tips of F2-F4, northern portion of F7, and F9 (Figs 3 and 9c). Fourth, SU3 thickens down relay zones developed between fault segments, such as observed along C5 and C9 in the southeast (Fig. 9c). Fifth, in the south, SU3 diverge toward and shows subtle thickening across the crestal faults between the F14 and C3-C4 (Fig. 4b-d). Sixth, lower part of SU3 has a wedge-shaped geometry and thickens toward C1-C2, while the upper part of the unit is cross-cut by the crestal faults above the C1-C2 (Fig. 4d). Seventh, although SU3 generally thickens across the faults, this unit shows a constant thickness and a tabular geometry across the lateral tips of some major basinward-dipping normal faults situated in the western area (F2, F8; Fig. 9c). Finally, SU3 thins, being upturned towards the mud pipe flanks and eroded within intra-SU3 and at the base of the overlying SU4 (E4-E5; Figs 4b, 6b and 9c).

7.5.2 Interpretation

Using thickness patterns in and the overall seismic-stratigraphic architecture of SU3, we can reconstruct the tectonic processes during the subsequent ca. 1.9 Myr post-rift history of the basin. Four key tectonic processes related to supra-shale extensional faulting occurred at this time. First, the existing normal faults continued to grow (F10-F14) via tip propagation (F2, F3-F4, F7 and C3) and locally, hard-linkage by relay-breaching (F3-F5, F7 and F9; Figs 9i and 10). As a result, both basinward- and landward-dipping normal faults have a final concave and convex-towards-the-basin geometry (Fig. 9i). Second, following thickness pattern and maximum displacements, formation of relay zone along C5, C8-C9 and nucleation of F4 and F6 occurred (Figs 9i, 10 and Table 5). Third, following growth of the F14, C3 and C4 and the subtle thickness pattern of the crestal faults, these crestal faults above rollover anticline nucleated in response to clockwise tilting of these listric faults (Fig. 9i). We interpret that the crestal faults were formed due to shearing above and during formation of the hanging-wall rollover associated with listric supra-shale faults (e.g. Dula, 1991; McClay, 1990). Fourth, during this time, some established faults like F2, F8, C1-C2, and C6-C7 underwent tip retreat or became inactive (Figs 9i and 10). More specifically, some faults are inactive due to: (i) cross-cutting by listric and crestal fault formations that are relatively younger (C1-C2; Fig. 4d), or; (ii) strain migration toward an incipient new footwall breaching of C8-C9 within a large soft-linked relay zone (C5-C9; Figs 4 and 8) (cf. Walsh et al., 1999; Imber et al., 2003).

These processes of fault growth and decay result in complex structural styles and evolution during the Upper?-uppermost Miocene in the shelf-edge of Tarakan Basin. We also noted a difference in the style of growth faulting during the Upper?-uppermost Miocene, being shown by: (i) a relatively simple series of basinward-dipping listric faults in the north, and a complex series of roller folds, basinward- and landward-dipping listric, with associated crestal, faults in the south (Fig. 9i); (ii) active listric faults, to that observed in Middle-Upper Miocene age, are located relatively landward in the north and basinward in the south (cf. Fig. 9h and 9i).

Four processes could explain these along-strike differences in structural style and kinematics. First, the landward-dipping listric fault may occurred due to reactivation of deeper thrust (e.g. Sapin et al., 2012). Yet, in Tarakan, we cannot see any thrust faults, underlaying the landward-dipping listric faults (Fig. 4).

Second, the difference in overburden structural styles reflects along margin change of shelf breaks, given that the landward-dipping listric fault tend to form near them (Ings and Beaumont, 2010). This interpretation appears consistent with along strike change of seabed scarp, reflecting by concave towards-the-basin geometry (Fig. 8d). This interpretation also infers that the distribution of landward-dipping listric faults and their flanking folds might continue northeastward beyond our dataset (Fig. 7). However, we exclude this model because, rather than the presence of the landward-dipping listric faults, a previous 2D seismic-based study document either basinward-dipping listric faults or landward-dipping shale-detached thrusts (Hidayati et al., 2007) (Fig. 1b).

Third, the process of horizontal compaction and fluid expulsion may have migrated along the margin. This interpretation is supported by: (i) base mobile-shale surface being deeper in the centre; and, (ii) mobile shale being thicker in the centre (Fig. 7). This interpretation seems to perhaps consistent with the interpretation of higher sediment accumulation rates in the north (120-500 m/my) than the south (100-330 m/my) (Fig. 2). In our view, the existence of higher sediment accumulation rates in the north relatively to the south indicate southward ductile flow of mobile shales.

The fourth explanation is that the difference in the styles reflects along-strike differences in the timing and magnitude of tilting of the mobile shales and their basal surface. Seaward tilting of this surface is up to 17^{o} in the north, whereas it is lower in the south ($4\text{-}7^{o}$) (cf. Figs 3 and 4). This interpretation is consistent, for example, with the study of Wu et al. (2015) and with the results from several physical models of shale-rich deltas (e.g. Mourgues et al., 2009), which suggest that landward-dipping listric fault systems are better developed when the dip of the mobile shales and their basal surface is relatively gentle.

Besides the overburden deformation, the SU3 growth strata also record a deformation linked to the mobilization of the shale unit in the southeast (E4-E5 and MP; Fig. 4b, 6b and 9c). Although it is not very clear, we suggest that the growth of the anticline in the southeast during the deposition of SU3 led to crestal collapse of overburden above the anticline, with the collapse providing pathways for the ascent of mobile shale, resulting in the emplacement of mud pipe (cf. a fluidized mud pipe of Morley, 2003a; Bonini and Mazzarini, 2010; Bonini, 2012) (SA and MP; Fig. 4b). This interpretation explains the spatial relationship between the fold hinge and the pipe, as well as the basinward and the northward (i.e., along-strike) flow of mobile shale.

7.6 Stratal unit 4 (Uppermost Miocene-Pliocene)

7.6.1 Description

SU4 thickens across F3-F7, F9, F12, F14, C3-C5, C8-C9 and down the associated relay zones (Fig. 9d). Although this unit shows local thickening in the hanging-wall of normal faults, relatively to that observed on underlaying strata, we also observe: (i) a constant thickness along the trace of many shale-detached (southern tips of F2, F8, F10-11, and F13) and crestal normal faults (along C3-C4; cf. Fig. 9c-d); and, (ii) thinning onto hanging-wall of C5 and C9 due to erosion at the base of the overlying unit, SU5 (E6; Figs 4 and 6b-c). The area of erosion trends sub-parallel to these faults (Fig. 9d).

SU4 varies in thickness adjacent to mud pipes and volcanoes in the southeast and the north of the study area (MP and MV; Fig. 9d). In the southeast, this unit is upturned towards and thins above the pipe crest (MP; Fig. 4b and Table 3). However, in the north, the upper interval of this unit shows chaotic reflections above the F5 (Fig. 3b and Table 3).

7.6.2 Interpretation

The seismic-stratigraphic patterns in SU4 are used to reconstruct the tectonic processes during the subsequent ca. 3.7 Myr post-rift history of the basin. The processes are illustrated by active listric faults during this time is located relatively landward in the north to that observed in Upper-Uppermost Miocene, while the faults continue to grow in the south (cf. Fig. 9i and 9j). These faults are shown by the on-going growth of F9, F3-F8, F14, C3, and C9 (Fig. 8j and 10). More specifically to the F4-F5, and F9, thickness patterns of the SU3 and SU4 show they grew via lengthening, and the later subsequently being followed by a hard-linkage (cf. Fig. 9c-d and 10). Fault growth and hanging-wall tilting was also associated with the erosion of previously deposited strata (e.g. C5 and C9; Fig. 9d, j). The erosion above the faults are consistent with the presence of Pliocene unconformity in NW Borneo (Kessler and Jong., 2017; Morley et al., 2021) (SEA91U; Fig. 2). We interpret that faults grew in response to continued progradation of the sedimentary wedge and related differential compaction of and fluid expulsion from the mobile shales (e.g. Van Rensbergen and Morley, 2000, 2003), with the latter process being particularly important in the south (i.e. F12, F13-F14; Fig. 9j). Some faults also underwent tip retreat and/or became inactive (e.g. F2, F8, F10-F11, F13; Fig. 9j and 10).

Variations in mobile shale-related deformation continued to occur along the margin during Upper Miocene-Pliocene, being illustrated by ongoing growth and initiation of mud diapirism in the southeast and north respectively (MP and MV; Fig. 9j).

7.7 Stratal unit 5 (Pliocene-Pleistocene)

7.7.1. Description

SU5 is broadly tabular, thickening locally towards F9, F10-F14 , and showing a wedge-shaped geometry toward the hanging-walls of F2-F7, C4-C5, and C9 (Figs 3-4). There are further local variations in thickness compared to what we observe in underlying strata. First, SU5 displays subtle thickening towards and along C4 and fault-related crestal grabens along C3 (Figs 4b-d and 9e). Second, this unit has a constant thickness across the southern tip of F2 and along hanging-wall of F3-F4 (Fig. 9e). Third, SU5 varies in thickness around F3-F4, F13, and along the crestal faults C3-C4 (Fig. 9e). These variations consistently appear with erosion of the top of the unit, being located in the hanging-wall of listric and crestal normal faults, and/or at the base of SU6 (label E7-E8; Figs 3a-b and 4).

SU5 also varies in thickness around mud pipes and volcanoes (Fig. 9e). In the southeast, the lower part of this unit thins and onlaps above SU4 toward the crest of a mud pipe, whereas the upper part of the unit thickens and wedges eastward (Figs 4b and 6b). In the north, however, SU5 show continuous mound shape geometries above the F6 (label MV; Fig. 3b).

7.7.2. Interpretation

The geometry of SU5 records the tectonic processes during the subsequent ca. 2.58 Myr post-rift history of the basin. Overburden extension continued as shown by the continued growth of F2-F7, F10-14, C3-C5 and C9, and the reactivation of some crestal normal faults above the C3-C4 (Figs 9k and 10). More specifically to the variations of thickness on F3-F4, F6-F7, F13 and along the crestal faults, their tilting was accompanied by erosion (label E7-E8; Figs 3a-b, 4 and 6c-d). The reactivation of crestal faults, however, are inferred due to another pulse of strata bending in response to clockwise hanging-wall rotation of the C3-C4 fault (Figs 4b-d and 9e). This reactivation shows that locus of faulting in the south, relatively to that observed in Uppermost Miocene-Pliocene, move basinward.

During the Pliocene-Pleistocene, the mud pipe in the south were buried (Fig. 9k). In the north, however, a mud volcano occurred (MV; Fig. 3b).

7.8 Stratal unit 6 (Pleistocene-Holocene)

7.8.1 Description

SU6, although show tabular and constant thickness adjacent many supra shale faults, still thickens across and/or is wedge-shaped in and diverges towards the hanging-walls of F3, F5-F7, F9, C3, C5 and C9 (Figs 4 and 9f). This unit also thins toward and onlap onto the mud volcano (Figs 3b and 9f).

7.8.2 Interpretation

SU6 record the latest tectonic activity in the margin, during the last 0.012 Myr. Tip retreat of many supra-shale faults occurred during this time (Fig. 9l), with many faults dying-out (Figs 3-5). However, some faults remained active (e.g. F3, F5-F6, C5 and C9; Fig. 9l), coincident with and possibly driven by, an increase in the rate of sediment accumulation (from 130 to 820 m/my) (Fig. 2). The mud volcano in the north, however, continued to grow via shale fed along fractures (MV; Fig. 9l).

8. Discussion

8.1 Structural styles in the Tarakan Basin

Previous 2D seismic-based studies show that NW-trending arches (e.g. Wight et al., 1993), NE-SW-striking thin-skinned normal and inverted listric, rollover folds, thick-skinned normal (e.g. Wight et al., 1993; Biantoro et al., 1996), and/or NW-SE-striking strike-slip faults (e.g. Lentini and Darman, 1996; Hidayati et al., 2007) are all developed in the Tarakan Basin (Fig. 1). All previous studies agree that Miocene gravity-driven failure led to listric faulting and related folding (e.g. Van Bemmelen, 1949; Hidayati et al., 2007). However, the post-Pliocene kinematic development of the arches and inverted listric faults mentioned above is debated, with two-end member models proposed: (i) the strike-slip faulting (Wight et al., 1993; Lentini and Darman, 1996; Balaguru et al., 2003; Hidayati et al., 2007); or (ii) the uplift of pre-existing rift-related topography (Sapiie et al., 2021; cf. Ahmed et al., 2022). These previous studies have, however, some important limitations. For example, (i) they lack a comprehensive map-view reconstruction of the base-mobile and supra-shale structures, characterizing key structures like fault tip lines and branch lines, sedimentary facies boundaries, and fold axes (e.g. Sylvester, 1988; Erdi and Jackson, 2022), which collectively make it possible to evaluate geometry and kinematic of the faults and the folds (e.g. Harding, 1990); and (ii) widely spaced (> 62.5 m) 2D seismic data mean it is hard to determine the geometry and evolution of inherently 3D structures such as segmented normal faults and geometrically complex shale structures (e.g. Tearpock and Bischke, 2002; Groshong, 2006; Ze and Alves, 2019).

Our detailed 3D seismic interpretation constrains the structural style and distribution of shale and supra-shale structures, showing many occur above NE-trending base mobile-shale surface that inferably has a concave-basinward geometry, and which are superimposed on a generally seaward-dipping surface (Fig. 11). Above this surface, the basal mobile shale unit shows extensional (e.g. shale rollers and shale-detached normal faults) and contractional (anticlines) structures. We also interpret that the mobile shale flowed upward, forming mud pipes and volcanoes that pierced a few kilometers of overburden strata and that were active until recently (i.e. they are locally expressed at the seabed). Supra-shale deformation consist of concave- and convex-basinward arrays of extensional listric growth faults, and related hanging-wall rollover folds and outer-arc bending-related crestal faults.

In our dataset we also observe the southern tip of the Bunyu Arch; this is a major structure previously described as a series of NW-trending folds (Figs 1 and 8; Wight et al., 1993; Lentini and Darman, 1996). In our view, rather than comprising several NW-trending folds, this structure is represented by several NE-trending rollover folds associated with large, shale-detached listric growth faults (Figs 8 and 9). Thus, in contrast to the previous interpretations, we suggest that other similar NW-trending folds or arches in the Tarakan Basin are *en echelon*, basement-detached rollover folds (Fig. 1).

In summary, we propose that the Neogene structural style of the Tarakan Basin reflects (Fig. 11): (i) variations in sediment accumulation rates and the progradation of deltaic sedimentary wedges from northeastern Borneo; (ii) the dominantly seaward flow of the basal shale unit (lowermost Middle Miocene) to induce inflation and diapirism of mobile shale unit in the distal domain, possibly with a contribution of margin-parallel flow to generate the large, central depocenter and drive mud pipes and volcanism in the south and north, respectively (Figs 6-7); (iii) the growth and linkage of the supra-shale extensional fault systems (Fig. 9); and (iv) associated gravitational failure of the Neogene sedimentary wedge, induced by irregular seaward tilting of the entire margin (Fig. 7a-b), driven by plate-scale uplift of Borneo (e.g. Hall, 2013).

8.2 Deltaic growth faulting: geometry, timing, and tectonic significance

Previous studies demonstrate that the geometry, distribution, and kinematics of growth faulting in shale-rich deltas are controlled by the interaction between gravity gliding downslope associated with margin uplift (e.g. Garfunkel, 1984; Gawthorpe et al., 1994; Wu and Bally, 2000) and sediment loading during delta progradation (e.g. Evamy, 1978; Cohen and McClay, 1996; McClay et al., 2003) above an overpressured shale (e.g. Mandl and Crans, 1981; Espurt et al., 2009; Mourgues et al., 2009; Lacoste et al, 2012; Fernández-Ibañez and Soto, 2017) and/or differential compaction (e.g. Fazlikhani and Back, 2015) and associated fluid expulsion (e.g.

Totterdell and Krassay, 2003; Van Rensbergen and Morley, 2000, 2003; Back and Morley, 2016). Still, fault growth and linkage (e.g. Fazlikhani and Back, 2012; 2017) and base mobile-shale slope angle (e.g. Wu et al, 2015; Lacoste et al., 2012) can also contribute to development of the growth faulting. Fault-related deformation can migrate basinward as the causal sedimentary wedge prograde (e.g. Evamy, 1978; Cohen and McClay, 1996; McClay et al., 2003; Espurt et al., 2009). The fault-related deformation can also migrate landward via either lateral fault-linkage (e.g. Imber et al., 2003; Fazlikhani and Back, 2012) or seaward tilting of the margin (e.g. Lacoste et al., 2012). Along margin change of shelf break and shale flow (Ings and Beaumont, 2010), reactivation of deeper thrust (Sapin et al., 2012), and/or variations in the dip of the seaward tilted base mobile-shale (Espurt et al., 2009; Wu et al., 2015) also controls the locus of faulting and the dip direction of the growth faults. More specifically to the tilting, an increase in the dip of base mobile-shales tends to produce basinward-dipping growth faults, whereas a relatively gently-dipping shale base usually promotes the formation of landward-dipping growth faults (e.g. Wu et al., 2015). Sediment loading can also promote the local escape of fluids and mud, forming the intrusion (e.g. pipes) and extrusion (e.g. volcanoes) of mobilized shales (e.g. Van Rensbergen and Morley, 2000; Back and Morley, 2016).

Our study shows that the distribution of landward- and basinward-dipping deltaic growth faulting varies in time and space along-strike change of the concave, shelf-edge region of the Tarakan Basin. The basinward-dipping listric faults are broadly developed across the study area, whereas the landward-dipping listric faults are preferentially developed above the surface that is defined by a relatively gentle dip (4-7^{o}) steps (Figs 3-4 and 10). The locus of basinward growth faulting is consistent with the study of Wu et al. (2015), given they show how domains with a gentle dip of the shale base tend to nucleate landward-dipping growth faults. Here we also demonstrate that active growth faulting migrates landward and basinward during the Neogene-to-Recent, possibly in response to varying sedimentation rates of the delta systems prograding from the eastern margin of Borneo (Figs 9 and 11). Landward migration of extensional faulting occurred above relatively steep-dipping base mobile-shale surface in the north, whereas basinward migration occurred above the relatively gentle-dipping base mobile-shale surface in the south. These inferences are also in agreement with (i) the lateral propagation and linkage of basinward-dipping listric faults in the north, and basinward- and landward-dipping listric faults in the south; and, (ii) uplift in north Borneo since Miocene (e.g. Hall, 2013).

9. **Conclusions**

We conducted a seismic-stratigraphic analysis of 3D seismic reflection data from the shelf-edge to upper slope of Tarakan Basin, offshore Indonesia to unravel the lateral variability in the structural style, distribution, and kinematics of thin-skinned, shale-related deformation. We showed that the Tarakan delta system, including its underlying basal mobile shale, is deformed by a range of shale structures (i.e. shale anticlines, mud pipes and volcanoes), and basinward-and landward-dipping growth faults located above and trending parallel to NE-trending base mobile-shale highs. Using seismic stratigraphy and isochore (thickness) maps we identified four main tectono-stratigraphic stages: (i) Eocene-early Middle Miocene? – continental rifting and deposition of the mobile shale unit; (ii) Middle-Upper Miocene? – fault nucleation, growth, and linkage in the proximal domain, and formation of a shale-cored anticline in a more distal area; (iii) Upper Miocene-Pliocene – lateral propagation and eventual retreat of the extensional faults, and mud diapirism; and (iv) Pleistocene-Holocene – extensional faults reactivation, decay and death, and mud volcanism. Our study suggests the temporal and spatial evolution of Neogene deformation in the shelf-edge to upper slope region of the Tarakan Basin reflects the interaction between variations in sediment accumulation rate and the progradation of deltaic sedimentary wedges, mobile shale flows, the growth and linkage of extensional fault, and the associated gravitational failure of the shale-rich delta above base mobile-shale surface. More specifically our study further highlights the key relationship between the direction of strain migration and the geometry of the base mobile-shale in gravity-driven deformation systems, with landward-directed migration occurring above regions defined by steeply seaward-dipping surface, and basinward-directed fault migration above relatively gentle basal surface. These learnings can provide insights into the structural styles and kinematics observed on other shale-rich margins, such as that characterizing the Mahakam and Niger deltas, and the Ceduna sub-basin in offshore South Australia.

Acknowledgment

The first author thanks Robert Hall, Perdana Rakhmana Putra, Danny Hilman Natawidjaya, Maruf Mukti, and Mudrik Rahmawan Daryono for scientific discussions in the early stage of this study. This study represents the PhD research of the first author, being sponsored by the Indonesia Endowment Fund for Education (LPDP) (Grant/Award Number: 201712220212151). This study is administratively supported by formerly Research Center for Geotechnology, Indonesian Institute of Science (LIPI) (now National Research and Innovation Agency, - BRIN). All author would like to thank Hamed Fazlikhani, an anonymous reviewer, and Christopher Morley for detailed and insightful reviews that improves this paper, as well as Atle Rotevatn for editorial handling. A big thank you to TGS for providing access to the high-quality 3D seismic dataset and for allowing publication of the results of this study. The authors also acknowledge Schlumberger for providing Petrel software to Imperial College London. JIS acknowledges the financial support of the Applied Geodynamics Laboratory (AGL) Industrial Associates program, comprising the following companies: BP, Chevron, Condor, ENI, ExxonMobil, Fairfield, Hess, Murphy, Oxy, Petrobras, Petronas, PGS, Repsol, RIPED, Rockfield, Shell, Talos, TGS, and Woodside Energy (http://www.beg.utexas.edu/agl/sponsors). Publication authorized by the Director, Bureau of Economic Geology, The University of Texas at Austin.

Table Captions

Table 1: Description of seismic datasets used in our study in Tarakan Basin, Offshore Indonesia.

Table 2: Characterization, seismic velocity, and tectonic significance of the interpreted seismic horizons of the Neogene section of the Tarakan Basin, offshore Indonesia, as seen in the shelf-edge and upper slope of the basin.

Table 3: Summary of the diagnostic seismic characteristics of the shale structures identified between the shelf-edge and upper slope of Tarakan Basin, offshore Indonesia. See also Table S1 in Appendix for a larger version of this table. Seismic data courtesy of TGS.

Table 4: Summary of principal characteristics of the supra-shale faults as are seen in the area between the shelf-edge and upper slope of Tarakan Basin, offshore Indonesia. See also Table S2 in Appendix for a larger version of this table. Seismic data courtesy of TGS.

Table 5: Maximum length and displacement of the studied faults in the Tarakan Basin, offshore Indonesia.

Figure captions

Figure 1: Regional tectonic map and profile of Tarakan Basin in offshore Indonesia (inset shows the general location of the area). Although precise location cannot be released due to confidentiality, the study is around the shelf-edge to upper slope of the extensional domain of this basin. (a) Simplified regional structural map illustrating key tectonic features in the north-east Borneo, consisting of Ahus (AA), Bunyu (BA), Tarakan (TA), Latih (LA) and Sebatik (SA) arches; major regional normal fault (MRNF), like the Maratua (MFZ) and Sampurna (SFZ) fault zones. Map compiling information from Wight et al. (1993), Lentini and Darman (1996), Moss et al. (1998), Hidayati et al. (2007), and Balaguru and Hall (2009). Well locations are taken from Wight et al. (1993), Corelab (2007), Chakhmakhchev and Rushworth (2010), and Rosary et al. (2014). Base elevation map is derived from GEBCO (2020). (b) Regional profile across the offshore Tarakan Basin (modified from Hidayati et al., 2007).

Figure 2: Regional tectono-stratigraphic framework chart of the Paleogene to Quaternary (Q) section in north-west and north-east Borneo (modified and simplified with information from

Hall, 2012, 2013, 2019). In this chart, the lithostratigraphy of Tarakan Basin (modified from Achmad and Samuel, 1984; Heriyanto et al., 1992) is simplified into syn-rift, mobile shale, and supra mobile-shale unit. The syn-rift and mobile shale unit are separated by a regional unconformity, which is called as the Deep Regional (DRU), South China Sea (SCSU) or Early Miocene (EMU) unconformity that have an Early-Middle Miocene age (Levell, 1987; Cullen, 2010, 2014; Madon et al., 2013). This chart is compared with the South East Asia eustatic sea level curve that records a global sea level drop (SEA59), and includes the position of two regional unconformities (SEA52U and SEA91U) (Morley et al., 2021) and the sediment accumulation rates for the Tarakan Basin derived according to well data (modified from Hidayati et al., 2007). It is also included our seismic horizons and units differentiated in the Neogene sequence of the shelf-edge of Tarakan Basin, offshore Indonesia. Well locations and source area of sediment budget are shown in Fig. 1. Noted that sediment accumulation rates have not been corrected for post-depositional, burial-related compaction, and in consequence they should be considered as minimum values.

Figure 3: Selected seismic profiles showing the configuration of the Tarakan Basin in a direction parallel to the regional dip (approximately 1-17°) of the mobile-shale base, which is parallel to bulk translation direction of the supra-shale cover. It is also illustrated the style of growth faulting and how it varies laterally in the northern part of the study area. Note that “E" marks the location of local unconformities and/or erosional truncations (see Fig. 6 for details). More specifically to Figure 3a, this profile is located close to the Vanda-1 well in the southeast of the profile, although due to confidentiality, the exact position of the well is omitted here. Uninterpreted version of the three seismic profiles are shown in Appendix S1. Seismic data courtesy of TGS.

Figure 4: Margin-perpendicular seismic profiles illustrating the styles of growth fault systems in the southern part of the study area. The W-E orientation of the four seismic lines (a–d) is sub-parallel to the regional dip (approximately 4-5°) of the base mobile-shale, and to the bulk translation direction of the supra-shale cover. Notes of “x” show layering of seismic facies that may reflect relict or new, deformation-related internal fabrics in the mobile shales. Notes of “E", however, reflect unconformities and/or erosional truncations (see Fig. 6 for details). Due

to confidentiality, the exact position of the seismic profiles (a–c) is omitted here. Uninterpreted version of the four seismic profile is shown in Appendix S1. Seismic data courtesy of TGS.

Figure 5: Composite, SW-NE margin-parallel seismic profile illustrating shale and supra-shale structural styles. This orientation is normal to the regional dip of the base of mobile shale and to the bulk translation direction of the sedimentary cover. This profile also shows the present relationship of the basin with the sub-shale sequences, which are deformed by high-angle normal faults related to the Paleogene continental rifting (Fig. 2). Notes of “x” show layering of seismic facies that may reflect relict or new, deformation-related internal fabrics in the mobile shales. Notes of “E", however, reflect unconformities and/or erosional truncations (see Fig. 6 for details). This profile is situated in the northeast, close to the position of the Vanda-1 well. Due to confidentiality, the exact position of well are omitted here. Uninterpreted version of the seismic profile is shown in Appendix S1. Seismic data courtesy of TGS.

Figure 6: Unconformities and truncations within study area. (a) Zoom in of Fig. 5 that highlights the occurrence of E1 unconformities at the top of H2. (b) Detailed window of Fig. 4a documenting the existence of various unconformities and/or erosional truncations (e.g. E3 and E6-E8 at the top of H4 toH7, respectively) in the hanging-wall of listric faults. (c) Detailed window of Fig. 4b showing diverse unconformities (e.g. E2 and E3, within SU2 and SU3, respectively) related to the fold growth of a shale anticline (SA) that contains a mud pipe (MP) in the crest. Note top of H4 is eroded by H5 above the MP, as shown by E4. (d) Detailed zoom in Fig. 3a highlighting the existence of unconformities (E8) in the hanging-wall of a listric fault in the north. Uninterpreted version of the seismic profile is shown in Appendix S1. Seismic data courtesy of TGS.

Figure 7: Base mobile-shale surface and mobile shale isochore maps. (a) Base mobile-shale structural map and (b) its interpretative sketch map, illustrating spatial geometry of base mobile-shale surface that reflects the inherited rift topography. The interpretative map (Fig. 7b) illustrates the geometry and distribution of N-S sub-shale faults, being drawn based on the map-view (Fig. 7a) and seismic profiles (Figs 3-5). (c) Mobile shale isochore map (in s TWT), illustrating morphology and distribution of shale in the basin. To compare, it is included the

distribution and type of structures affecting the top of mobile shale (TMB), including shale roller and anticline (see Table 3 for description of these shale structures).

Figure 8: Overburden structural maps of the main supra-shale seismic reflections: (a) H2 – Middle Miocene, (b) H4 – Uppermost Miocene, (c) H7 – Upper Pleistocene, and (d) seabed (Fig. 2). These maps contain information regarding structures affecting the supra-shale sequences, as basinward and landward normal faults, but also mobile shale structures like mud pipes and mud volcanoes. Table 3 and 4 contain a detailed description of the seismic expression and the differentiating characteristics of these structures.

Figure 9: Overburden isochore maps of all the supra-shale seismic units differentiated in this study (Fig. 2): (a) SU1 – Middle Miocene; (b) SU2 – Middle-Upper Miocene; (c) SU3 – Upper-Uppermost Miocene; (d) SU4 – Uppermost Miocene-Pliocene; (e) SU5 – Pliocene-Pleistocene; (f) SU6 – Pleistocene-Holocene, accompanied in (g-l) by their tectonic interpretation. These interpretative sketches illustrate the Neogene tectonic evolution of the Tarakan Basin in the study area, detailing the activity of shale and supra-shale structures at every particular time. Note on these maps, we also drawn erosional truncation that are observed from Figs 3-6. See also Appendix of S2 for a larger version of overburden isochore and their interpretative sketches.

Figure 10: Synoptic plot illustrating length development of active and inactive (i.e. n/a) faults over fault history, being measured from isochore data (Fig. 9). Some faults established their maximum length early (e.g. F1-F2, F14-16, and C4), while other increased their length via lengthening/tip propagations (e.g. F13, C1 and C7) and/or lateral hard-linkage (e.g. F3-F12, C2-C3, C5-C6 and C8-C9). More specifically to C4, active lengths is separated by inactivity, showing fault reactivation.

Figure 11: Regional map summarizing the main findings of our study and the structural elements that controlled the Neogene evolution of the offshore area of Tarakan Basin, north-east Borneo. The main findings include the distribution and role played of supra-shale growth faulting (basinward and/or landward normal faults), the inferred flow pattern of mobile shales, the distal shale inflation and contraction, as well as the occurrence of steps in the base

of mobile shales that delineate structural highs. The inferred shale trough reflects structural low of base mobile-shale, where the local thickest mobile shale present in shelf-edge of the offshore area. The inferred seaward boundary of shale-detached thrust and landward boundary of growth faults is taken from Hidayati et al. (2007).

Data Availability Statement

The seismic data supporting the findings of this study are available from TGS. However, restrictions apply to the availability of these data, which were used under license for this study.

References

Achmad, Z., & Samuel, L. (1984). *Stratigraphy and depositional cycles in the N.E. Kalimantan Basin.* Paper presented at the Indonesian Petroleum Association, 13th Annual Convention and Exhibition Jakarta, Indonesia.

Abdulah, F.A., Akbarsyah, M.S.A.A., Yuniardi, Y.Y., 2016. Clay mineral effect in sandstone reservoir toward usage of fluid drilling type. Study case - Lisa Field, Tarakan Basin. 78th EAGE Conference and Exhibition 2016, 1–5. https://doi.org/10.3997/2214-4609.201600787.

Advokaat, E.L., Marshall, N.T., Li, S., Spakman, W., Krijgsman, W., van Hinsbergen, D.J.J. (2018). Cenozoic rotation history of Borneo and Sundaland, SE Asia revealed by paleomagnetism, seismic tomography, and kinematic reconstruction. Tectonics, 37, 2486–2512. https://doi.org/10.1029/2018TC005010.

Ahmed, B., McClay, K., Scarselli, N., & Bilal, A. (2022). New insights on the gravity-driven deformation of late Albian – early Turonian stacked delta collapse systems in the Ceduna sub-basin, Bight Basin, southern margin of Australia. *Tectonophysics*, 229184. https://doi.org/10.1016/j.tecto.2021.229184

Back, S., & Morley, C. K. (2016). Growth faults above shale – Seismic-scale outcrop analogues from the Makran foreland, SW Pakistan. *Marine and Petroleum Geology, 70*, 144-162. https://doi.org/10.1016/j.marpetgeo.2015.11.008

Balaguru, A. (2008). Tectonic evolution, sedimentation and chronostratigraphic chart of Sabah, Malaysia. *European Association of Geoscientists & Engineers, PGCE 2008*, cp-258-00078. https://doi.org/10.3997/2214-4609-pdb.258.P28

Balaguru, A., & Hall, R. (2009). *Tectonic Evolution and Sedimentation of Sabah, North Borneo, Malaysia*. Paper presented at the AAPG International and Exhibition Cape Town, South Africa

Balaguru, A., Nichols, G., & Hall, R. (2003). The origin of the 'circular basins' of Sabah, Malaysia. *Bulletin of the Geological Society of Malaysia, 46*, 335-351.

Biantoro, E., Kusuma, M.I., and Rotinsulu, L.F. (1996). *Tarakan sub-basin growth faults, North-East Kalimantan: Their roles in previous hydrocarbon entrapment*. Indonesian Petroleum Association, 25th Annual Convention Proceedings, 1, 175–189

Bonini, M. (2012). Mud volcanoes: Indicators of stress orientation and tectonic controls. *Earth-Science Reviews, 115*(3), 121-152. https://doi.org/10.1016/j.earscirev.2012.09.002

Bonini, M., & Mazzarini, F. (2010). Mud volcanoes as potential indicators of regional stress and pressurized layer depth. *Tectonophysics, 494*(1), 32-47. https://doi.org/10.1016/j.tecto.2010.08.006

Briggs, S. E., Davies, R. J., Cartwright, J. A., & Morgan, R. (2006). Multiple detachment levels and their control on fold styles in the compressional domain of the deepwater west Niger Delta. *Basin Research, 18*(4), 435-450. https://doi.org/10.1111/j.1365-2117.2006.00300.x

Brondijk, J.F., 1962. A reclassification of a part of the Setap Shale Formation as the Temburong Formation. British Borneo Geol. Survey Ann. Rept., 56-60

Brun, J.-P., & Mauduit, T. P. O. (2008). Rollovers in salt tectonics: The inadequacy of the listric fault model. *Tectonophysics, 457(1),* 1-11. https://doi.org/10.1016/j.tecto.2007.11.038

Brun, J.-P., & Mauduit, T. P. O. (2009). Salt rollers: Structure and kinematics from analogue modelling. *Marine and Petroleum Geology, 26*(2), 249-258. https://doi.org/10.1016/j.marpetgeo.2008.02.002

Cartwright, J. A., Trudgill, B. D., & Mansfield, C. S. (1995). Fault growth by segment linkage: an explanation for scatter in maximum displacement and trace length data from the Canyonlands Grabens of SE Utah. *Journal of Structural Geology, 17*(9), 1319-1326. https://doi.org/10.1016/0191-8141(95)00033-a

Chakhmakhchev, A., & Rushworth, P. (2010). *Global overview of recent exploration investment in deepwater - New discoveries, plays and exploration potential.* Paper presented at the AAPG Convention, Calgary, Alberta, Canada.

Chima, K. I., Granjeon, D., Do Couto, D., Leroux, E., Gorini, Ch., Rabineau, M., & Mora-Glukstad, M. (2022). Tectono-stratigraphic evolution of the offshore western Niger Delta from the Cretaceous to present: Implications of delta dynamics and paleo-topography on gravity-driven deformation. *Basin Research, 34*(1), 25-49. https://doi.org/10.1111/bre.12609

Cohen, H. A., & McClay, K. (1996). Sedimentation and shale tectonics of the northwestern Niger Delta front. *Marine and Petroleum Geology, 13*(3), 313-328. https://doi.org/10.1016/0264-8172(95)00067-4

CoreLab (2007). Core Laboratories Indonesia Regional Datasets. In: Corelab (Ed.). Retrieved from: https://corelab.com/irs/cms/docs/Indonesia_Regional_Datasets_Sept2007.pdf

Cullen, A. (2014). Nature and significance of the West Baram and Tinjar Lines, NW Borneo. *Marine and Petroleum Geology, 51*, 197-209. https://doi.org/10.1016/j.marpetgeo.2013.11.010

Cullen, A., Reemst, P., Henstra, G., Gozzard, S., & Ray, A. (2010). Rifting of the South China Sea: new perspectives. *Petroleum Geoscience, 16*(3), 273. https://doi.org/10.1144/1354-079309-908

Damuth, J. E. (1994). Neogene gravity tectonics and depositional processes on the deep Niger Delta continental margin. *Marine and Petroleum Geology*, 11(3), 320-346. https://doi.org/10.1016/0264-8172(94)90053-1

Dawers, N. H., Anders, M. H., & Scholz, C. H. (1993). Growth of normal faults: Displacement-length scaling. *Geology*, 21(12), 1107-1110. https://doi.org/10.1130/0091-7613(1993)021<1107:gonfdl>2.3.co;2

Dula, W. F., Jr. (1991). Geometric Models of Listric Normal Faults and Rollover Folds1. *AAPG Bulletin, 75*(10), 1609-1625. https://doi.org/10.1306/0C9B29B1-1710-11D7-8645000102C1865D

Elsley, G. R., & Tieman, H. (2010). A Comparison of Prestack Depth and Prestack Time Imaging of the Paktoa Complex, Canadian Beaufort MacKenzie Basin. In: Wood, L. J. (Ed.), Shale Tectonics (Vol. 93, pp. 79-90): American Association of Petroleum Geologists, Memoir. https://doi.org/10.1306/13231309M933419

Erdi, A., & Jackson, C. A. -L. (2021). What controls salt-detached contraction in the translational domain of the outer Kwanza Basin, offshore Angola? *Basin Research, 33*(3), 1880-1905. https://doi.org/10.1111/bre.12539

Erdi, A., & Jackson, C. A. -L. (2022). Salt-detached strike-slip faulting, Outer Kwanza Basin, Offshore Angola. *Tectonics*, 41, e2022TC007428. https://doi.org/10.1029/2022TC007428

Espurt, N., Callot, J.-P., Totterdell, J., Struckmeyer, H., & Vially, R. (2009). Interactions between continental breakup dynamics and large-scale delta system evolution: Insights from the Cretaceous Ceduna delta system, Bight Basin, Southern Australian margin. *Tectonics, 28*(6), TC6002. https://doi.org/10.1029/2009TC002447

Evamy, B. D., Haremboure, J., Kamerling, P., Knaap, W. A., Molloy, F. A., & Rowlands, P. H. (1978). Hydrocarbon Habitat of Tertiary Niger Delta. *AAPG Bulletin, 62*(1), 1-39. https://doi.org/10.1306/C1EA47ED-16C9-11D7-8645000102C1865D

Fagin, S. (1996). The fault shadow problem: Its nature and elimination. *The Leading Edge, 15*(9), 1005-1013. https://doi.org/10.1190/1.1437403.

Fazlikhani, H., & Back, S. (2012). Temporal and lateral variation in the development of growth faults and growth strata in western Niger Delta, Nigeria. *AAPG Bulletin, 96*(4), 595-614. https://doi.org/10.1306/08291111023

Fazlikhani, H., & Back, S. (2012). Temporal and lateral variation in the development of growth faults and growth strata in western Niger Delta, Nigeria. AAPG Bulletin, 96(4), 595-614. https://doi.org/10.1306/08291111023

Fazlikhani, H., & Back, S. (2015a). The influence of differential sedimentary loading and compaction on the development of a deltaic rollover. Marine and Petroleum Geology, 59, 136-149. https://doi.org/10.1016/j.marpetgeo.2014.08.005

Fazlikhani, H., & Back, S. (2015b). The influence of pre-existing structure on the growth of syn-sedimentary normal faults in a deltaic setting, Niger Delta. *Journal of Structural Geology, 73*, 18-32. https://doi.org/10.1016/j.jsg.2015.01.011

Fazlikhani, H., Back, S., Kukla, P. A. & Fossen, H. (2017). Interaction between gravity-driven listric normal fault linkage and their hanging-wall rollover development: a case study from the western Niger Delta, Nigeria. *Geological Society, London, Special Publications, 439(1),* 169. DOI: 10.1144/SP439.20

Fernández-Ibáñez, F., & Soto, J. I. (2017). Pore pressure and stress regime in a thick extensional basin with active shale diapirism (western Mediterranean). *AAPG Bulletin*, *101*(2), 233–264. https://doi.org/10.1306/07131615228

Francis, A. (2018). A simple gGuide to seismic depth conversion: Part I. *GeoExpro, 15,* 24.

Franke, D., Barckhausen, U., Heyde, I., Tingay, M., & Ramli, N. (2008). Seismic images of a collision zone offshore NW Sabah/Borneo. *Marine and Petroleum Geology, 25*(7), 606-624. https://doi.org/10.1016/j.marpetgeo.2007.11.004

Garfunkel, Z. (1984). Large-scale submarine rotational slumps and growth faults in the Eastern Mediterranean. *Marine Geology, 55(3),* 305-324. https://doi.org/10.1016/0025-3227(84)90074-4

Gawthorpe, R. L., Fraser, A. J. & Collier, R. E. L. (1994). Sequence stratigraphy in active extensional basins: implications for the interpretation of ancient basin-fills. *Marine and Petroleum Geology, 11(6), 642-658.* https://doi.org/10.1016/0264-8172(94)90021-3

Ge, H., Jackson, M. P. A., & Vendeville, B. C. (1997). Kinematics and dynamics of salt tectonics driven by progradation. *AAPG Bulletin, 81*(3), 398-423. https://doi.org/10.1306/522B4361-1727-11D7-8645000102C1865D

GEBCO Bathymetric Compilation Group (2020). *The GEBCO_2020 Grid - a continuous terrain model of the global oceans and land*. Retrieved from: http://www.gebco.net

Graves, J. E. & Swauger, D. A. (1997). Petroleum Systems of the Sandakan Basin, Philippines. In: Howes, J.V.C., Noble, R.A. (Eds.), Petroleum Systems of SE Asia and Australasia. Indonesian Petroleum Association, Jakarta, pp. 799-813

Groshong, R. H., Jr. (2006). 3-D structural geology. A practical guide to quantitative surface and subsurface map interpretation 2nd. Ed. Springer-Verlag, Berlin, 400 pp. https://doi.org/10.1007/978-3-540-31055-6

Hall, R. (2012). Late Jurassic–Cenozoic reconstructions of the Indonesian region and the Indian Ocean. *Tectonophysics, 570-571*, 1-41. https://doi.org/10.1016/j.tecto.2012.04.021

Hall, R. (2013). Contraction and extension in northern Borneo driven by subduction rollback. *Journal of Asian Earth Sciences, 76*, 399-411. https://doi.org/10.1016/j.jseaes.2013.04.010

Hall, R. (2019). The subduction initiation stage of the Wilson cycle. In: Wilson, R. A., Houseman, G. A., McCaffrey, K. J. W., Doré, A. G., & Buiter, S. J. H.(Eds.), *Fifty Years of the Wilson Cycle Concept in Plate Tectonics*. Geological Society, London, Special Publications, 470, 415–437. https://doi.org/10.1144/SP470.3

Hall, R., & Nichols, G. J. (2002). Cenozoic sedimentation and tectonics in Borneo: climatic influences on orogenesis. In: Jones, S. J., & Frostick, L. (Eds.), *Sediment Flux to Basins: Causes, Controls and Consequences.* Geological Society, London, Special Publication, 191, 5–22. https://doi.org/10.1144/GSL.SP.2002.191.01.02

Hansen, J. P. V., Cartwright, J. A., Huuse, M., & Clausen, O. R. (2005). 3D seismic expression of fluid migration and mud remobilization on the Gjallar Ridge, offshore mid-Norway. *Basin Research, 17*(1), 123-139. https://doi.org/10.1111/j.1365-2117.2005.00257.x

Harding, T. P. (1990). Identification of wrench faults using subsurface structural data: Criteria and pitfalls. *AAPG Bulletin, 74*(10), 1590-1609. https://doi.org/10.1306/0C9B2533-1710-11D7-8645000102C1865D

Heriyanto, N., Satoto, W., & Sardjono, S. (1992). *An overview of hydrocarbon maturity and its migration aspects in Bunyu Island, Tarakan Basin.* Paper presented at the Indonesian Petroleum Association, 21st Annual Convention and Exhibition Jakarta, Indonesia.

Hidayati, S., Guritno, E., Argenton, A., Ziza, W., & Del Campana, I. (2007). *Re-Visited Structural Framework of the Tarakan Sub-Basin Northeast Kalimantan-Indonesia.* Paper presented at the Proceedings, Indonesian Petroleum Association, 31st Annual Convention and Exhibition

Hongbin, Xiao & Suppe, J. (1992) Origin of Rollover. *AAPG Bulletin, 76*(4), 509-529. DOI: 10.1306/BDFF8858-1718-11D7-8645000102C1865D

Hudec, M. R., & Soto, J I. (2021). Piercement Mechanisms for Mobile Shales. *Basin Research, 33,* 2862–2882. https://doi.org/10.1111/bre.12586

Hutchison, C.S., 1996. The 'Rajang Accretionary Prism' and 'Lupar Line' problem of Borneo. In: Hall, R., & Blundell, D. J. (Eds.), *Tectonic Evolution of SE Asia*. Geological Society, London, Special Publication, 106, 247–261. https://doi.org/10.1144/GSL.SP.1996.106.01.16

Hutchison, C. S. (2005). *Geology of North West Borneo: Sarawak, Brunei and Sabah*. Amsterdam, Elsevier.

Imber, J., Childs, C., Nell, P. A. R., Walsh, J. J., Hodgetts, D., & Flint, S. (2003). Hanging wall fault kinematics and footwall collapse in listric growth fault systems. *Journal of Structural Geology, 25*(2), 197-208. https://doi.org/10.1016/s0191-8141(02)00034-2

Ings, S. J. & Beaumont, C. (2010). Continental margin shale tectonics: preliminary results from coupled fluid-mechanical models of large-scale delta instability. *Journal of the Geological Society,167(3)*, 571. DOI: 10.1144/0016-76492009-052

Jackson, C. A. L., Bell, R. E., Rotevatn, A., & Tvedt, A. B. M. (2017). Techniques to determine the kinematics of synsedimentary normal faults and implications for fault growth models. In: Childs, C., Holdsworth, R. E., Jackson, C. A.-L., Manzocchi, T., Walsh, J. J., & Yielding, G. (Eds.), *The Geometry and Growth of Normal Faults.* Geological Society, London, Special Publications, 439, 187-217. https://doi.org/10.1144/sp439.22

Jackson, M. P. A., & Hudec, M. R. (2017). *Salt tectonics: principles and practice*. Cambridge, Cambridge University Press.

Jamaludin, S.N.F., Sautter, B., Pubellier, M., and Beg, M.A. (2021). The succession of Upper Eocene-Upper Miocene limestone growth and corresponding tectonic events in Luconia Shelf, Sarawak, Malaysia. Frontiers in Earth Science, 9, 588629. http://doi.org/10.3389/feart.2021.588629.

Johnson, P. W., & Hansen, K. (1987). *Method for calibrating stacking velocities for use in time-depth conversion*. Paper presented at the Offshore Technology Conference. https://doi.org/10.4043/5403-MS

Kessler, F.L. & Jong, J. (2017). The roles and implications of several prominent unconformities in Neogene sediments of the greater Miri area, NW Sarawak. Warta Geol. 43 (4), 1–8.

Kopf, A. J. (2002). Significance of mud volcanism. *Reviews of Geophysics, 40*(2), 2-1-2-52. https://doi.org/10.1029/2000RG000093

Krisnabudhi, A., Sapiie, B., Riyanto, A.M., Gunawan, A., & Rizky, F.F. (2022). Mesozoic-Cenozoic stratigraphy and tectonic development of the Southern Great Tarakan Basin, Northeast Borneo, Indonesia. *Rudarsko-geološko-naftni zbornik, 37*(1), 123-138. https://doi.org/10.17794/rgn.2022.1.11

Lacoste, A., Vendeville, B. C., Mourgues, R., Loncke, L., & Lebacq, M. (2012). Gravitational instabilities triggered by fluid overpressure and downslope incision – Insights from analytical and analogue modelling. *Journal of Structural Geology, 42*, 151-162. https://doi.org/10.1016/j.jsg.2012.05.011

Lentini, M. R., & Darman, H. (1996). *Aspects of the Neogene tectonic history and hydrocarbon geology of the Tarakan Basin.* Paper presented at the Indonesian Petroleum Association, 25th Annual Convention and Exhibition, Indonesia.

Levell, B.K., 1987. The nature and significance of regional unconformities in the hydrocarbon–bearing Neogene sequence offshore West Sabah. Geological Society of Malaysia, 21, 55–90.

Liu, Z., Wang, H., Hantoro, W.S., Sathiamurthy, E., Colin, C., Zhao, Y., and Li, J. (2012). Climatic and tectonic controls on chemical weathering in tropical Southeast Asia (Malay Peninsula, Borneo, and Sumatra). Chemical Geology, 291, 1–12. https://doi.org/10.1016/j.chemgeo.2011.11.015.

Lunt, P. and Madon, M. (2017). Onshore to offshore correlation of northern Borneo; a regional perspective. *Bulletin of the Geological Society of Malaysia*, 64 (1), 101-122. DOI: 10.7186/bgsm64201710

Li, Ch., Luo, X., Zhang, L., Fan, C., Xu, Ch., Liu, A., Li, H., Li, J., & Lei, Y. (2022). New understanding of overpressure responses and pore pressure prediction: Insights from the effect of clay mineral transformations on mudstone compaction. *Engineering Geology, 297*, 106493. https://doi.org/10.1016/j.enggeo.2021.106493

Madon, M., Kim, Ch. L., & Wong, R. (2013). The structure and stratigraphy of deepwater Sarawak, Malaysia: Implications for tectonic evolution. *Journal of Asian Earth Sciences, 76*, 312–333. https://doi.org/10.1016/j.jseaes.2013.04.040

Mandl, G., & Crans, W. (1981). Gravitational gliding in deltas. In: McClay, K. R., & Price, N. J. (Eds.), *Thrust and nappe tectonics*. Geological Society, London, Special Publications, 9, 41–54. https://doi.org/10.1144/GSL.SP.1981.009.01.05

Mansfield, C. S., & Cartwright, J. (1996). High resolution fault displacement mapping from three-dimensional seismic data: evidence for dip linkage during fault growth. *Journal of Structural Geology, 18*(2-3), 249-263. https://doi.org/10.1016/S0191-8141(96)80048-4

Maulin, H.B., Sapiie, B., and Gunawan, I. (2019). *The Neogene deformation, unconformity surfaces and uplift features in delta tectonics, Tarakan Sub Basin*. Proceedings, Indonesian Petroleum Association, Forty-Third Annual Convention & Exhibition, September 2019, paper no. IPA19-G-191.

Maulin, H. B., Sapiie, B., & Gunawan, I. (2021). Analisis Sesar Tumbuh Pada Sistem Tektonik Delta Tersier di Subcekungan Tarakan, Kalimantan Utara. *Bulletin of Geology, 5*(2), 570-579.

McClay, K. R. (1990). Extensional fault systems in sedimentary basins: a review of analogue model studies. *Marine and Petroleum Geology, 7*(3), 206-233. https://doi.org/10.1016/0264-8172(90)90001-W

McClay, K., Dooley, T., & Zamora, G. (2003). Analogue models of delta systems above ductile substrates. In: Van Rensbergen, P., Hillis, R. R., Maltman, A. J., & Morley, C. K. (Eds.) *Subsurface sediment mobilization*. Geological Society, London, Special Publications, 216, 411–428. https://doi.org/10.1144/GSL.SP.2003.216.01.27

McGrath, A. G., & Davison, I. (1995). Damage zone geometry around fault tips. *Journal of Structural Geology, 17*(7), 1011-1024. https://doi.org/10.1016/0191-8141(94)00116-H

Mitchum, R. M., Jr., Vail, P. R., & Sangree, J. B. (1977). Seismic stratigraphy and global changes of sea level, Part 6: Stratigraphic interpretation of seismic reflection patterns in depositional sequences. In: Payton, C. E. (Ed.), *Seismic Stratigraphy — Applications to Hydrocarbon Exploration* . American Association of Petroleum Geologists, Memoir, 26, 117–133. https://doi.org/10.1306/M26490C8

Morley, C. K. (2003a). Mobile shale related deformation in large deltas developed on passive and active margins. In: Van Rensbergen, P., Hillis, R.R., Maltman, A.J., & Morley, C.K. (Eds.) *Subsurface sediment mobilization*. Geological Society, London, Special Publications, 216, 335-357. https://doi.org/10.1144/GSL.SP.2003.216.01.22

Morley, C. K. (2003b). Outcrop examples of mudstone intrusions from the Jerudong anticline, Brunei Darussalam and inferences for hydrocarbon reservoirs. *Geological Society, London, Special Publications*, 216 (1), 381-394. DOI: 10.1144/GSL.SP.2003.216.01.25

Morley, C. K. (2007). Development of crestal normal faults associated with deepwater fold growth. *Journal of Structural Geology, 29*(7), 1148-1163. https://doi.org/10.1016/j.jsg.2007.03.016

Morley, C. K., & Guerin, G. (1996). Comparison of gravity-driven deformation styles and behavior associated with mobile shales and salt. *Tectonics, 15*(6), 1154-1170. https://doi.org/10.1029/96TC01416

Morley, C. K. & Westaway, R., 2006. Subsidence in the super-deep Pattani and Malay basins of Southeast Asia: a coupled model incorporating lower-crustal flow in response to post-rift sediment loading. *Basin Research*, 18, 51–84. https://doi.org/10.1111/j.1365-2117.2006.00285.x

Morley, C. K., King, R., Hillis, R., Tingay, M. & Backe, G. (2011). Deepwater fold and thrust belt classification, tectonics, structure and hydrocarbon prospectivity: A review. *Earth-Science Reviews, 104 (1)*, 41-91. DOI: https://doi.org/10.1016/j.earscirev.2010.09.010

Morley, R. J., Morley, H. P., Swiecicki, T., (2017). Constructing Neogene palaeogeographical maps for the Sunda region. Proceedings of the South East Asia Petroleum Exploration Society (SEAPEX) Conference, April 2017.

Morley, R.J., Hasan, S.S., Morley, H.P., Jais, J.H.M., Mansor, A., Aripin, M.R., Nordin, M.H., and Rohaizar, M.H., (2021). Sequence biostratigraphic framework for the Oligocene to Pliocene of Malaysia: Highfrequency depositional cycles driven by polar glaciation. Palaeogeography, Palaeoclimatology, Palaeoecology, 561, 110058. https://doi.org/10.1016/j.palaeo.2020.110058.

Moss, S. J., Carter, A., Baker, S., & Hurford, A. J. (1998). A Late Oligocene tectono-volcanic event in East Kalimantan and the implications for tectonics and sedimentation in Borneo. *Journal of the Geological Society, 155*(1), 177–192. https://doi.org/10.1144/gsjgs.155.1.0177

Mourgues, R., Lecomte, E., Vendeville, B., & Raillard, S. (2009). An experimental investigation of gravity-driven shale tectonics in progradational delta. *Tectonophysics, 474*(3), 643-656. https://doi.org/10.1016/j.tecto.2009.05.003

Netherwood, R., & Wight, A. (1992). *Structurally-controlled, linear reefs in a Pliocene delta-front setting, Tarakan Basin, Northeast Kalimantan*. Paper presented at the Carbonate Rocks and Reservoirs of Indonesia: A Core Workshop.

Noon, S., Harrington, J., and Darman, H. (2003). *The Tarakan Basin, East Kalimantan: Proven Neogene fluvio-deltaic, prospective deep-water and Paleogene plays in a regional stratigraphic context*. Proceedings, Indonesian Petroleum Association, Twenty-Ninth Annual Convention & Exhibition, October 2003, paper no. IPA03-G-136.

Nur' Aini, S., Hall, R. & Elders, C. (2005). *Basement Architecture and Sedimentary Fill of The North Makassar Straits Basin*. Proceedings, Indonesian Petroleum Association, 30th Annual Convention & Exhibition, August 2005, paper no. IPA05-G-161

Putra, P. R., Tasiyat, Sapiie, B., & Ramadhan, A. M. (2017). *Pore pressure prediction and its relationship to structural style in Offshore Tarakan Sub-Basin, Northeast Kalimantan.* Paper presented at the Indonesian Petroleum Association, 41st Annual Convention and Exhibition Jakarta, Indonesia, paper no. IPA17-523-G.

Ramberg, H. (1981). The role of gravity in orogenic belts. Geological Society, London, Special Publications, 9, 125-140. https://doi.org/10.1144/GSL.SP.1981.009.01.11

Rangin, C., & Silver, E. (1991). Neogene tectonic evolution of the Celebes-Sulu Basins : New insights from Leg 124 drilling. *In:* Silver, E. A., Rangin, C., von Breymann, M. T., et al. (Eds.), *Proc. ODP, Sci. Results,* 124: College Station, TX (Ocean Drilling Program), 51–63. https://doi.org/10.2973/odp.proc.sr.124.122.1991

Rouby, D., Nalpas, T., Jermannaud, P., Robin, C., Guillocheau, F. & Raillard, S. (2011). Gravity driven deformation controlled by the migration of the delta front: The Plio-Pleistocene of the Eastern Niger Delta. *Tectonophysics, 513(1),* 54-67. https://doi.org/10.1016/j.tecto.2011.09.026

Rosary, D., Nicaksana, A. B., & Wilkinson, J.K. (2014). *A correlation of climate stratigraphy with biostratigraphy to confirm stratigraphic units in the Sebatik Area*. Proceedings, Indonesian Petroleum Association, 38th Annual Convention & Exhibition, May 2014, paper no. IPA14-G-258

Rowan, M.G., 2020. Salt- and shale-detached gravity-driven failure of continental margins, in: Scarselli, N., Adam, J., Chiarella, D. (Eds.), Regional geology and tectonics: Principles of geologic analysis, 2nd. Edition, Volume 1: Principles of geologic analysis. Elsevier, 205-234. https://doi.org/10.1016/B978-0-444-64134-2.00010-9.

Santos Betancor, I., & Soto, J. I. (2015). 3D geometry of a shale-cored anticline in the western South Caspian Basin (offshore Azerbaijan). *Marine and Petroleum Geology, 67*, 829-851. https://doi.org/10.1016/j.marpetgeo.2015.06.012

Sapin, F., Ringenbach, J.-C., Rives, T., & Pubellier, M. (2012). Counter-regional normal faults in shale-dominated deltas: Origin, mechanism and evolution. *Marine and Petroleum Geology, 37*(1), 121-128. https://doi.org/10.1016/j.marpetgeo.2012.05.001

Sapiie, B., Furqan, T. A., Septama, E., Wardaya, P. D., & Gunawan, I. (2021) Mechanism of gravity-driven deformation using sandbox modeling: A case study of the Tarakan Sub-Basin, East Kalimantan. Paper presented at the Indonesian Petroleum Association, 45th Annual Convention and Exhibition Jakarta, Indonesia, September 2021, paper no. IPA21-G-286.

Satyana, A.H., Nugroho, D., and Surantoko, I. (1999). Tectonic controls on the hydrocarbon habitats of the Barito, Kutei, and Tarakan Basins, Eastern Kalimantan, Indonesia: major dissimilarities in adjoining basins. Journal of Asian Earth Sciences, 17, 99–122. https://doi.org/10.1016/S0743-9547(98)00059-2

Satyana, A. H. (2015). *Rifting History of The Makassar Straits: New Constraints from Wells Penetrating the Basement and Oils Discovered in Eocene Section - Implications for Further Exploration of West Sulawesi Offshore*. Proceedings, Indonesian Petroleum Association 39th Annual Convention & Exhibition, May 2015, paper no. IPA15-G-104

Schlüter, H. U., Hinz, K., & Block, M. (1996). Tectono-stratigraphic terranes and detachment faulting of the South China Sea and Sulu Sea. *Marine Geology, 130*(1), 39-78. https://doi.org/10.1016/0025-3227(95)00137-9

Silver, E., & Rangin, C. (1991). Development of the Celebes Basin in the context of Western Pacific marginal basin history. *In:* Silver, E. A., Rangin, C., von Breymann, M. T., et al. (Eds.), *Proc. ODP, Sci. Results,* 124: College Station, TX (Ocean Drilling Program), 39–49. https://doi.org/10.2973/odp.proc.sr.124.121.1991

Situmorang, B. (1982). *The Formation of the Makassar Basin as Determined from Subsidence Curves*. Proceedings, Indonesian Petroleum Association 11th Annual Convention & Exhibition, June 1982

Soto, J. I., Fernández-Ibáñez, F., Talukder, A. R., & Martínez-García, P. (2010). Miocene Shale Tectonics in the Northern Alboran Sea (Western Mediterranean). In: Wood, L. J. (Ed.), *Shale Tectonics.* American Association of Petroleum Geologists, Memoirs, 93, 119–144. https://doi.org/10.1306/13231312M933422

Soto, J. I., Heidari, M., & Hudec, M. R. (2021a). Proposal for a mechanical model of mobile shales. *Scientific Reports, 11*(1), 23785. https://doi.org/10.1038/s41598-021-02868-x

Soto, J. I., Hudec, M. R., Mondol, N. H., & Heidari, M. (2021b). Shale transformations and physical properties—Implications for seismic expression of mobile shales. *Earth-Science Reviews*, 103746. https://doi.org/10.1016/j.earscirev.2021.103746

Spakman, W. and Hall., R. (2010). Surface deformation and slab-mantle interaction during Banda arc subduction rollback. *Nature Geosci, 3*, 562-566. https://doi.org/10.1038/ngeo917

Sylvester, A G. (1988). Strike-slip faults. *GSA Bulletin, 100*(11), 1666-1703. https://doi.org/10.1130/0016-7606(1988)100<1666:SSF>2.3.CO;2

Tearpock, D. J. & Bischke, R.E. (2002). Applied subsurface geological mapping with structural methods, 2nd. Ed. Pearson Education, 864 pp.

Tingay, M. R. P., Hillis, R. R., Swarbrick, R. E., Morley, C. K. & Damit, A. R., (2009). Origin of overpressure and pore-pressure prediction in the Baram province, Brunei. *AAPG Bulletin, 93 (1)*, 51-74. DOI: 10.1306/08080808016

Totterdell, J.M. & Krassay, A.A. (2003). The role of shale deformation and growth faulting in the Late Cretaceous evolution of the Bight Basin, offshore southern Australia In: Van Rensbergen, P., Hillis, R. R., Maltman, A. J., & Morley, C. K. (Eds.) *Subsurface sediment mobilization*. Geological Society, London, Special Publications, 216, 429-442. https://doi.org/10.1144/GSL.SP.2003.216.01.28

Van Bemmelen, R. W. (1949). *The Geology of Indonesia*: The Government Printing Office, The Hague.

Van Rensbergen, P., & Morley, C. K. (2000). 3D Seismic study of a shale expulsion syncline at the base of the Champion delta, offshore Brunei and its implications for the early structural evolution of large delta systems. *Marine and Petroleum Geology, 17*(8), 861-872. https://doi.org/10.1016/S0264-8172(00)00026-X

Van Rensbergen, P., Morley, C. K., Ang, D. W., Hoan, T. Q., & Lam, N. T. (1999). Structural evolution of shale diapirs from reactive rise to mud volcanism: 3D seismic data from the Baram delta, offshore Brunei Darussalam. *Journal of the Geological Society, 156*(3), 633-650. https://doi.org/10.1144/gsjgs.156.3.0633

Van Rensbergen, P., & Morley, C. K. (2003). Re-evaluation of mobile shale occurrences on seismic sections of the Champion and Baram deltas, offshore Brunei. In: Van Rensbergen, P., Hillis, R. R., Maltman, A. J., & Morley, C. K. (Eds.) *Subsurface sediment mobilization*. Geological Society, London, Special Publications, 216, 395–409. https://doi.org/10.1144/GSL.SP.2003.216.01.26

Van Hattum, M. W. A., Hall, R., Pickard, A. L., & Nichols, G. J. (2013). Provenance and geochronology of Cenozoic sandstones of northern Borneo. *Journal of Asian Earth Sciences, 76*, 266-282. https://doi.org/10.1016/j.jseaes.2013.02.033

Walsh, J. J., Bailey, W. R., Childs, C., Nicol, A., & Bonson, C. G. (2003). Formation of segmented normal faults: a 3-D perspective. *Journal of Structural Geology, 25*(8), 1251-1262. https://doi.org/10.1016/s0191-8141(02)00161-x

Walsh, J. J., & Watterson, J. (1988). Analysis of the relationship between displacements and dimensions of faults. *Journal of Structural Geology, 10*(3), 239–247. https://doi.org/10.1016/0191-8141(88)90057-0

Walsh, J. J., Watterson, J., Bailey, W. R., & Childs, C. (1999). Fault Relays, bends, and branch-lines. *Journal of Structural Geology, 21*(8–9), 1019–1026. https://doi.org/10.1016/S0191-8141(99)00026-7

Watkinson, I. M., & Hall, R. (2017). Fault systems of the eastern Indonesian triple junction: Evaluation of Quaternary activity and implications for seismic hazards. In: Cummins, P. R., & Meilano, I. (Eds.), *Geohazards in Indonesia: Earth Science for Disaster Risk Reduction* (Vol. 441, pp. 71–120): The Geological Society of London. https://doi.org/10.1144/SP441.8

Wight, A. W. R., Hare, L. H., & Reynolds, J. R. (1993). Tarakan Basin, NE Kalimantan, Indonesia: a century of exploration and future hydrocarbon potential. *Bulletin of the Geological Society of Malaysia, 33*, 263-288. https://doi.org/10.7186/bgsm33199319

Wu, S., Bally, A. W. (2000). Slope tectonics-comparisons and contrasts of structural styles of salt and shale tectonics of the northern Gulf of Mexico with shale tectonics of offshore Nigeria in Gulf of Guinea, in: Mohriak, W., & Talwani, M. (Eds.), *Atlantic Rifts and Continental Margins.* Geophysical Monograph-American Geophysical Union, 115, 151-172

Wu, J. E., McClay, K., & Frankowicz, E. (2015). Niger Delta gravity-driven deformation above the relict Chain and Charcot oceanic fracture zones, Gulf of Guinea: Insights from analogue models. Marine and Petroleum Geology, 65, 43-62. https://doi.org/10.1016/j.marpetgeo.2015.03.008

Ze, T., & Alves, T. M. (2019). Impacts of data sampling on the interpretation of normal fault propagation and segment linkage. *Tectonophysics, 762*, 79-96. https://doi.org/10.1016/j.tecto.2019.03.013

Zhang, J., Wu, S., Hu, G., Yue, D., Xu, Z., Chen, Ch., Zhang, K., Wang, J., & Wen, S. (2021). Role of Shale Deformation in the structural development of a deepwater gravitational system in the Niger Delta. *Tectonics, 40*(5), e2020TC006491. https://doi.org/10.1029/2020TC006491

Table

Table 1

Data	TBB-11 (Southern area)	TBN-10 (Northern area)
Date of acquisition and processing	2011-2012	2011-2012
Type/Processing	3D Kirchhoff Pre-Stack Time Migration (PSTM) seismic data	
Total area (km^2)	1316	1625
Water depth (m)	200-500	15-400
Inline orientation	N-S trending	NE-SE trending
Seismic dimension (m)	49039 x 60036	45290 x 70909
Vertical sample rate (ms)	2	2
Line spacing (m)	25	25
Vertical resolution	25 m at seabed	21 m at seabed
	250 m at 8710 ms	208 m at 7069 ms

1287 Table 2

Horizon	Interval Velocity (m/s)	Time	Seismic Character	Interpretation
H7	1500-3010	Upper Pleistocene (~0.012 Ma)	Parallel, very strong positive amplitude reflector observed in the S. It is locally as a chaotic, moderately medium-to-weak reflector in the NE.	H7 illustrating top of the youngest angular unconformity, being shown by truncation (labelled E8; Figs 3-4 and 6b-c). Associated to rollover folds within strata in the S (Fig. 9e, k).
H6	1700-3100	Lower Pleistocene (~1.8 Ma)	Parallel-to-sub parallel, low-to-medium positive amplitude reflector across the study area. It shows locally diverge eastward in the SE.	H6 illustrating angular unconformity in the SE, being shown by truncation (labelled E7; Figs 4 and 6c; cf. Unconformity II of Maulin et al., 2019).
H5	2100-3100	Pliocene (~2.6 Ma)	Parallel-to-wavy, very strong positive amplitude reflector in the S. Moderately chaotic reflector in the NE, and weak reflector and diverge eastward in the NE and SE.	H5 illustrating angular unconformity in the SE, being shown by truncation (labelled E6; Figs 4 and 6b-c; cf. Horizon II; Levell, 1987; Horizon A ; Franke et al., 2008; SEA91U of Morley et al., 2021).
H4	2400-3200	Upper most Miocene (~6.3 Ma)	Parallel strong positive amplitude reflector in the S. A moderate medium-weak, wavy and chaotic reflector in the NE and SE.	H4 illustrating angular unconformity in the SE, being shown truncation (labelled E3; Figs 3-4 and 6b-c; cf. unconformity I of Maulin et al., 2019). Associated to

				rollover folds in the S (Fig. 9c, i).
H3	3000-3200	Upper Miocene? (~8.2 Ma?)	Parallel-to-wavy, strong negative amplitude reflector.	H3 recording distribution rollover fold within strata in the northwest area (Fig. 9b, h).
H2	2900-3300	Middle Miocene? (~13.8 Ma?)	Parallel-to-sub parallel, strong positive amplitude reflector in the N. It is a chaotic, moderate medium-strong reflector in the S.	H2 illustrating angular unconformity in the central part, being shown by onlap or downlap of overlying stratal (labelled E1; Fig 5 and 6a).
TMB (Mobile shale)	3100-3500	Middle Miocene? (~14.8 Ma?)	Parallel-to-sub parallel negative amplitude reflector that marks transition between overburden and underlying mobile-shales. The mobile shales are seen as chaotic, weak-to-moderate amplitude reflections or as a domain with loss of reflectivity. Locally, its internal fabric shows cross-cutting reflections (label X in Figs 4 and 5).	Seismic facies of the mobile-shales (TMB) are either interpreted due to overpressure and/or to severe destruction of the fabric by deformation at critical-state conditions (Soto et al., 2021b). It cannot be excluded the existence of relict fabrics and/or seismic noise due to inaccurate seismic processing and acquisition (Elsley and Tieman, 2011; Li and Mitra, 2020).

H1	3300-3500	Eocene-to-late Early Miocene (~16-33 Ma)	Positive reflection in the S and N, while it is discontinuously imaged in the centre due to data coverage.	H1 illustrating top of syn-rift unit that mark unconformity (Deep Regional Unconformity; Levell, 1987 or South China Sea Unconformity; Cullen, 2010, 2014; SEA52U of Morley et al., 2021) of Early Miocene or Middle Miocene age (Hutchison, 2005; Madon et al., 2013). This reflection marks the base of mobile-shales and is also the top of deep half grabens bounded by thick-skinned extensional faults.

Table 3

Name	Shale Roller (SR)	Shale Anticline (SA)	Mud Pipe (MP)	Mud Volcano (MV)
Example	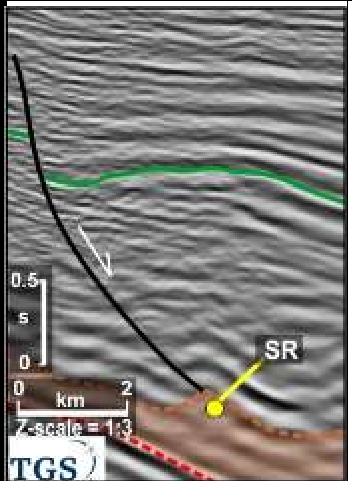	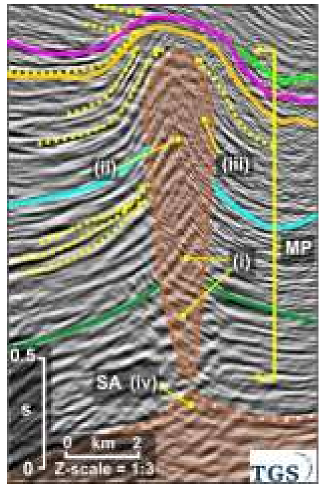		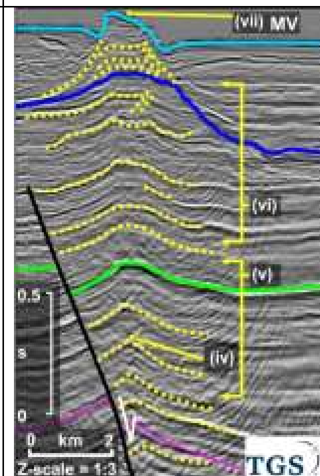
Seismic character	Broadly weak, sub-parallel-to-dipping chaotic reflector above mobile shale.	Chaotic, weak-to-moderate, amplitude reflections of mobile shale forming a structural high (label iv) with continuous supra shale reflections.	Cross-cutting chaotic reflections rise from the high (label i), being overlaid by significantly upturn, isolated low-amplitude, chaotic reflections (label ii). The chaotic reflections limited by a transitional zone of weak reflections (label iii).	Conical edifice with some internal reflectivity. Not clear feeders, although high angle normal faults and roller folds are commonly seen below the mud volcano.
Diagnostic description	An asymmetric, low amplitude triangular profile, comprising of a gentle and a relative steep-dipping flank that bound depocenter. On map view, it is reflected by an elongated thick mobile shale, parallel to the bounding normal fault (Figs 7c).	A low amplitude, large wavelength anticline. On map view, it is accompanied by an elongated domain of thick mobile shales.	H2-H3 are pierced by a mud-pipe body. On map view, it is seen as an elliptical domain that is defined by folding that affect H2-H4 (Figs 8a-b).	The reflections form a mounded structure between intra H5 and seabed (label v-vii). On map view, it is reflected by an asymmetric elliptical conical edifice usually seen between H5 and seabed in the north (Figs 8c-d).
Trend	NE-to-N			
Length (km)	≤ 80	≤ 12	≤ 11	≤ 3
Width (km)	≤ 5	≤ 4.3	≤ 2	≤ 1.5
Height (s)	≤ 1.2 (2.8 km)	≤ 0.6 (1.5 km)	≤ 3 (5 km)	≤ 1.9 (2.6 km)
Supra-shale faults association	Rollover and basinward-dipping or counter-regional normal fault with a listric and planar geometry.	N/A	N/A	Normal faults below the mud volcano

Driving mechanism	Reactive piercement (e.g. Hudec and Soto, 2021).	Contraction and/or horizontal flow of mobile shale (cf. Santos Betancor and Soto, 2015; Back and Morley, 2016).	Piercement produced by fluid migration along fractures, generated above the fold crest (H3-H4) (e.g. Santos Betancor and Soto, 2015; Hudec and Soto, 2021).	Piercement produced by fluid and shale migration along fractures in the lower interval (H5-intra H7) (e.g. Hudec and Soto, 2021), being followed upward by H7-seabed (e.g. Hansen et al., 2005).

Key: (H7) Upper Pleistocene (H6) Lower Pleistocene (H5) Pliocene (H4) Upper most Miocene (H3) Upper Miocene (H2) Middle Miocene Top Mobile Shale (TMB) (H1) Early Miocene

Table 4

Name	Example	Diagnostic description	Dip/ Plunge direction	Length (km)	Dip (o)	Max. throw (s)	Fault	Stra-tigraphic Architecture	Processes
Shale-detached normal fault (labelled SN)	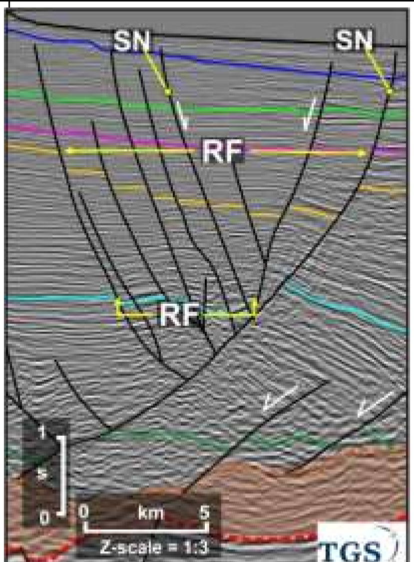	Listric or planar normal growth faults: Listric faults are detached along a surface below nearly horizontal stratum. In map view, they have both concave and convex geometries.	Basinward and landward (counter-regional)	≤ 53 (see Table 5 for more detailed)	30-86	≤ 2.8 (see Table 5 for more detailed)	Normal offset generally at H2-H6. The lower fault tips are within the mobile shales	SU1-SU6 thicken toward fault plane, forming a fault-bound depocenter.	Reactive piercement (e.g. Morley and Guerin, 1996; Hudec and Soto, 2021). Progressive prograding sedimentary loading (sedimentary-driven mechanism; e.g. Ge et al., 1997; Jackson et al., 2015, Back and Morley, 2016)
		Planar normal faults form symmetric and asymmetric grabens, above roll-over folds. In map view, the faults are parallel to the master listric faults.	Basinward and landward	≥ 1.9	60-85	≤ 0.1	Normal offset at H2-H6. The lower fault tips either die out downward into the supra shale sequence or form a physical-linkage with the listric fault	SU3-SU6 subtle thicken toward fault plane	Outer arc bending due to folding (e.g. Hongbin and Suppe, 1992; Imber et al, 2003; Erdi and Jackson, 2021).

Rollover fold (labelled RF)		Anticlines affecting an asymmetric wedge thickening toward the master fault. In map view, they are characterized by a broad-to-wide geometry (i.e. ratio of amplitude and half-wavelength=0.21-0.53) where axial fold surface is oriented parallel to the shale-detached normal fault. Locally, they have oblique linkage folds.	Basinward and landward	≤ 43	≤ 8 away and ≤ 13 toward master faults	N/A	N/A	SU2-5 thicken and bend toward the listric fault, and commonly thin outward.	Differential rate between sedimentation and fault slip (e.g. Dula, 1991; Hongbin and Suppe, 1992; Imber et al, 2003; Fazlikhani and Back, 2015a).

Key: (H7) Upper Pleistocene (H6) Lower Pleistocene (H5) Pliocene (H4) Uppermost Miocene (H3) Upper Miocene (H2) Middle Miocene Top Mobile Shale (TMB) (H1) Early Miocene

Table 5

Fault Name	Locations in the study area	Maximum Length	Maximum throws (ms TWT)	Figures
F1	North	40.1 km at SU1	1553 ms TWT (2.86 km) at top of H2	3c, 8a, 9a, 9g
F2	North	20.38 km at SU2	1000 ms TWT (1.5 km) at top of H3	3a-b, 8, 9a-e, 9h-l
F3	North	44.35 km at SU4	1554 ms TWT (2.3 km) at top of H3	3a-b, 6d, 8, 9a-f, 9h-l
F4	North		892 ms TWT (1.3 km) at top of H3	3c, 5, 8a-b, 9a-e, 9h-l
F5	North	35.13 km at SU4	488 ms TWT (0.73 km) at top of H3	3b-c, 5, 8, 9a-f, 9h-l
F6	North		951 ms TWT (1.14 km) at top of H4	3a-b, 5, 8, 9a-f, 9i-l
F7	North	63.12 km at SU3	1559 ms TWT (2.3 km) at top of H3	3b-c, 5, 6a, 8, 9a-f, 9h-l
F8	North		1250 ms TWT (2.06 km) at top of H2	4a, 5, 6a, 8a-b, 9a-e, 9g-l
F9	North		1125 ms TWT (1.35 km) at top of H4	3a-b, 8, 9a-f, 9i-l
F10	South	53 km at SU2	875 ms TWT (1.44 km) at top of H2	4a,8a-b, 9a-e, 9g-l
F11	South		776 ms TWT (1.28 km) at top of H2	4b-c, 5, 8a-b, 9a-e, 9g-l
F12	South		255 ms TWT (0.4 km) at top of H2	4d, 8a-b, 9a-e, 9g-l
F13	South	24.25 km at SU3	780 ms TWT (1.28 km) at top of H2	4b-c, 8-9
F14	South	9.5 km at SU1	375 ms TWT (0.6 km) at top of H2	4d, 8, 9a-e, 9g-l
F15	South	10.78 km at SU1	316 ms TWT (0.52 km) at top of H2	4b-c, 6b, 8a, 9a-b, 9g-h
F16	South	9.1 km at SU1	194 ms TWT (0.32 km) at top of H2	4c, 8a, 9a-b, 9g-h
C1	South	8.73 km at SU2	226 ms TWT (0.37 km) at top of H2	4d, 8a-b, 9a-c, 9g-i
C2	South	29.81 km at SU2	247 ms TWT (0.4 km) at top of H2	4d, 8a-b, 9a-c, 9g-i
C3	South		430 ms TWT (0.7 km) at top of H2	4b-d, 8-9
C4	South	19.77 km at SU5	360 ms TWT (0.4 km) at top of H4	4d, 8b, 9c-e, 9i-l
C5	South	28 km at SU2	230 ms TWT (0.34 km) at top of H3	4a-c, 8, 9a-f, 9h-l
C6	South		365 ms TWT (0.6 km) at top of H2	4d, 8a, 9a-b, 9g-i
C7	South	16.3 km at SU2	427 ms TWT (0.7 km) at top of H2	4d, 8a, 9a-b, 9g-h
C8	South	23.76 km at SU3	648 ms TWT (0.7 km) at top of H4	4d, 8a-b, 9a-e, 9i-l
C9	South		344 ms TWT (0.4 km) at top of H4	4c-d, 8, 9c-f, 9i-l

Figures

Figure 1

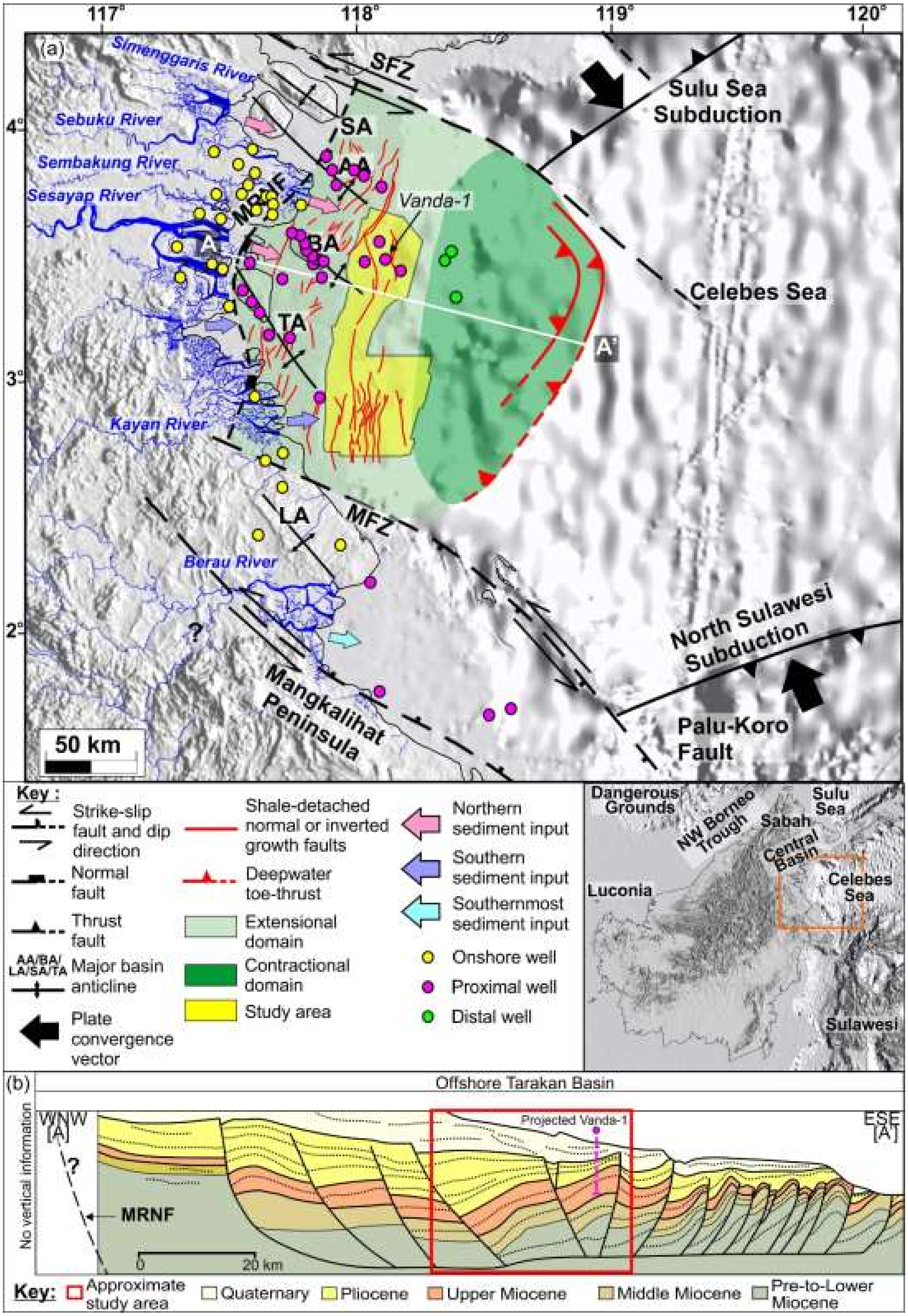

1299 Figure 2

1300

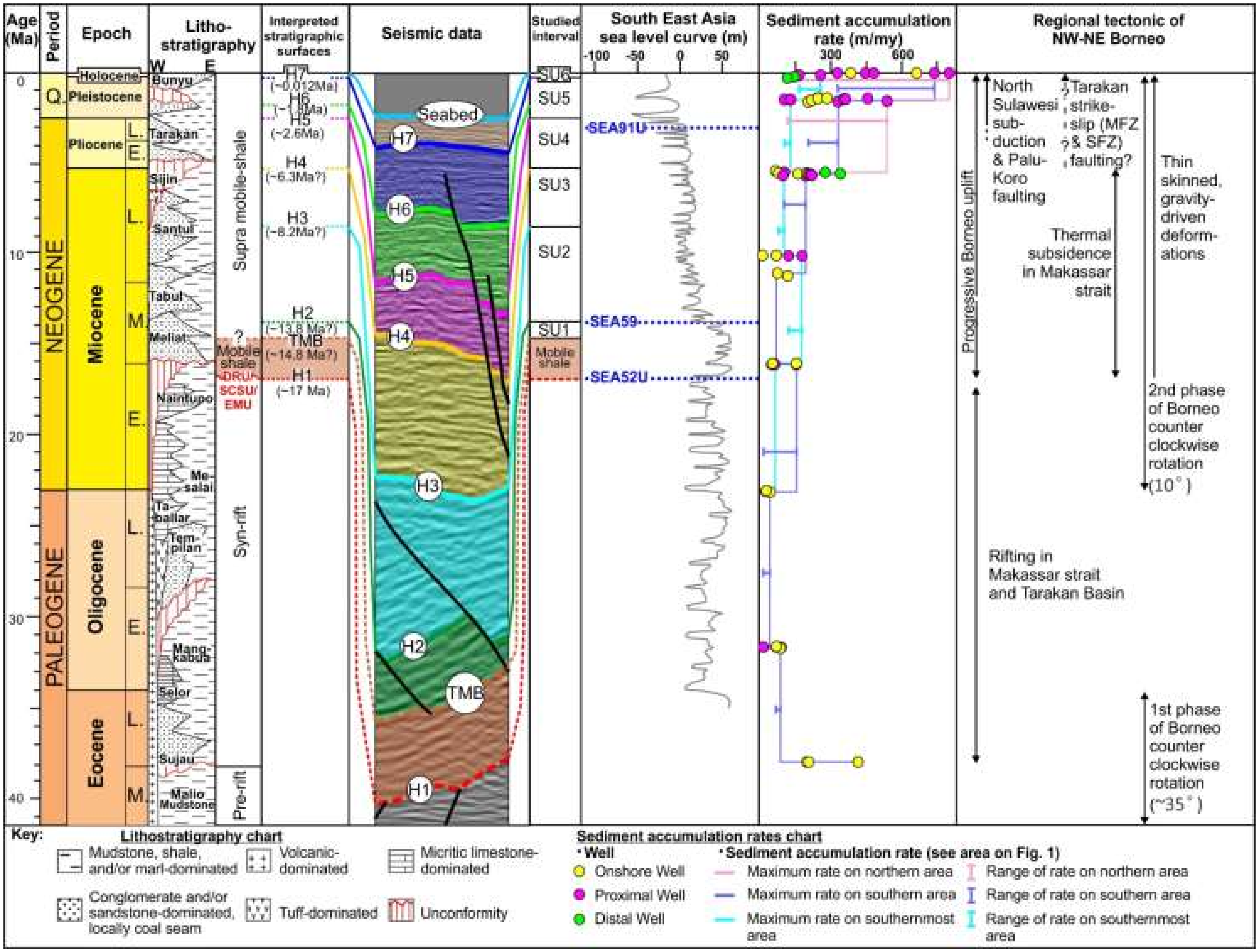

1301

1302 Figure 3

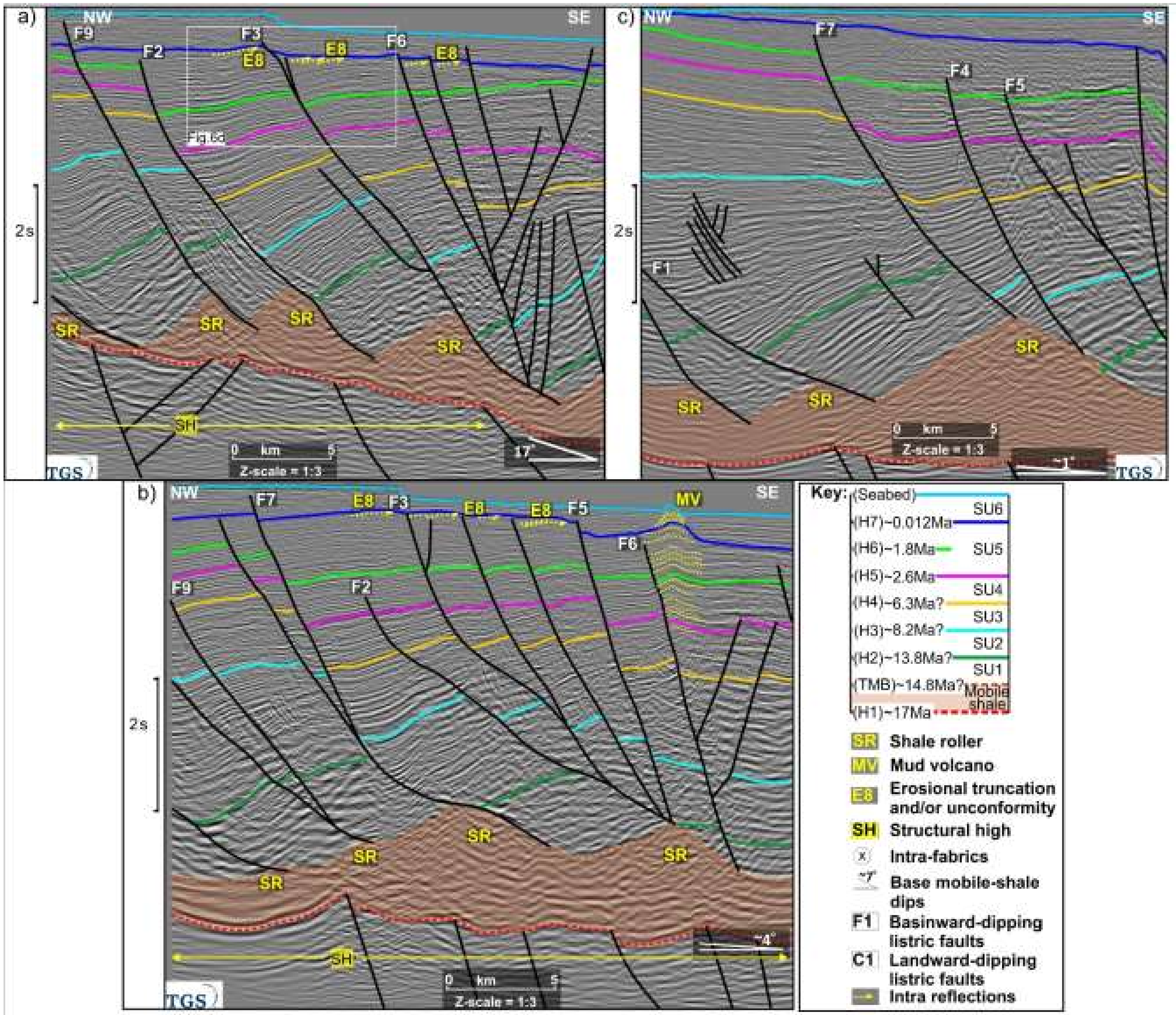

1303

Figure 4

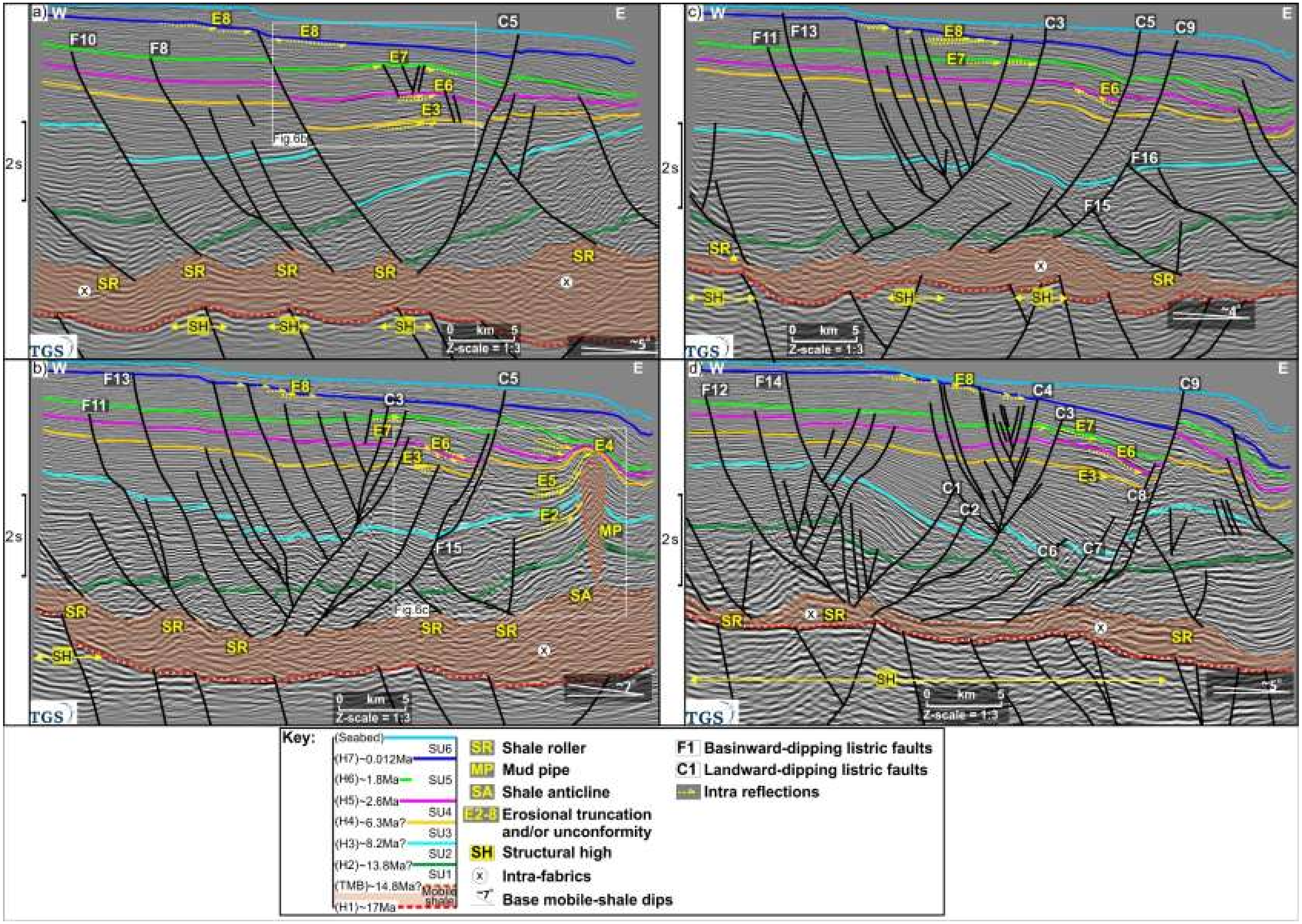
a) W
E
E8
E8
C5
F10
F8
E7
E6
E3
Fig.6b
2s
SR
SR
SR
SR
SR
SR
SH
SH
SH
0 km 5
Z-scale = 1:3
~5°
TGS
c) W
E
F11
F13
E8
C3
C5
C9
E7
E6
F16
F15
SR
SR
SH
SH
SH
~4°
b) W
E
F13
E8
C5
C3
F11
E7
E6
E3
E4
E5
E2
MP
F15
SA
Fig.6c
SR
SR
SR
SR
SR
SH
~7°
d) W
E
F12
F14
E8
C4
C9
C3
E7
E6
E3
C1
C2
C8
C6
C7
SR
SR
SR
SH
Key:
(Seabed)
SU6
(H7)~0.012Ma
(H6)~1.8Ma
SU5
(H5)~2.6Ma
SU4
(H4)~6.3Ma?
SU3
(H3)~8.2Ma?
SU2
(H2)~13.8Ma?
SU1
(TMB)~14.8Ma?
Mobile shale
(H1)~17Ma
SR Shale roller
MP Mud pipe
SA Shale anticline
E2-8 Erosional truncation and/or unconformity
SH Structural high
Intra-fabrics
~7° Base mobile-shale dips
F1 Basinward-dipping listric faults
C1 Landward-dipping listric faults
Intra reflections

Figure 5

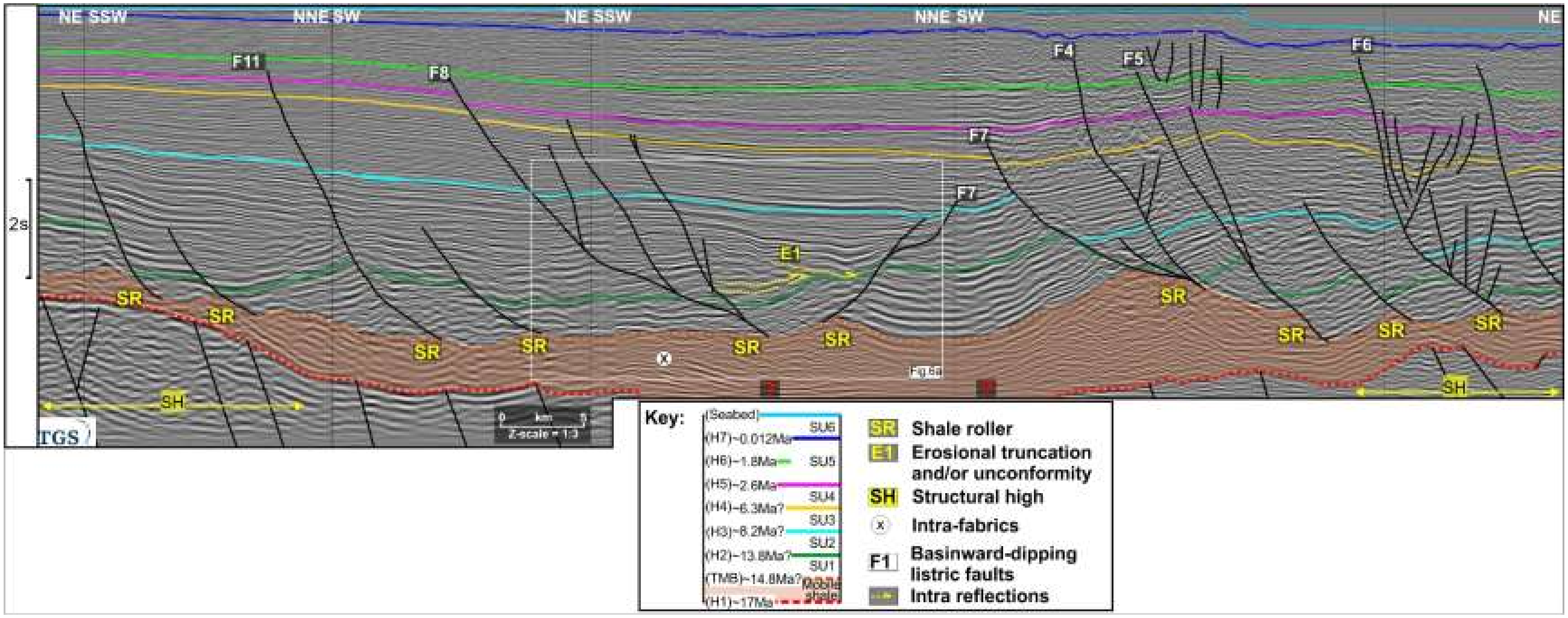

NE SSW
NNE SW
NE SSW
NNE SW
NE
F11
F8
F7
F7
F4
F5
F6
2s
E1
SR
SH
Fig 5b
TGS
0 km 5
Z-scale = 1:3
Key:
(Seabed)
(H7)~0.012Ma
(H6)~1.8Ma
(H5)~2.6Ma
(H4)~6.3Ma?
(H3)~8.2Ma?
(H2)~13.8Ma?
(TMB)~14.8Ma?
(H1)~17Ma
SU6
SU5
SU4
SU3
SU2
SU1
Mobile shale
SR Shale roller
E1 Erosional truncation and/or unconformity
SH Structural high
Intra-fabrics
F1 Basinward-dipping listric faults
Intra reflections

Figure 6

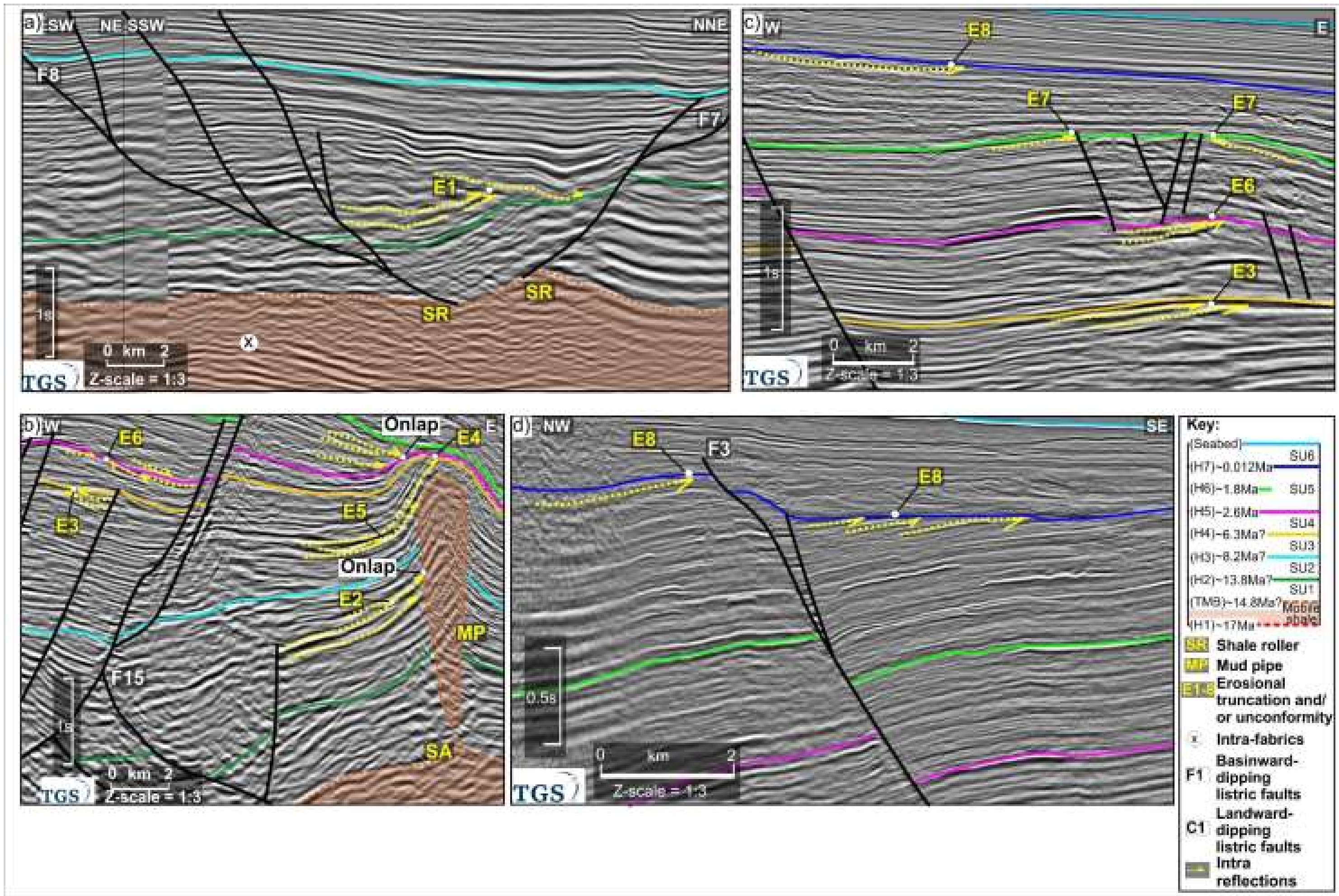
a) SSW
NE SSW
NNE
F8
F7
E1
SR
SR
1s
0 km 2
Z-scale = 1:3
TGS
c) W
E
E8
E7
E7
E6
E3
1s
0 km 2
Z-scale = 1:3
TGS
b) W
E
Onlap
E4
E6
E3
E5
Onlap
E2
MP
F15
1s
SA
0 km 2
Z-scale = 1:3
TGS
d) NW
SE
E8
F3
E8
0.5s
0 km 2
Z-scale = 1:3
TGS
Key:
(Seabed)
SU6
(H7)~0.012Ma
SU5
(H6)~1.8Ma
(H5)~2.6Ma
SU4
(H4)~6.3Ma?
SU3
(H3)~8.2Ma?
SU2
(H2)~13.8Ma?
SU1
(TMB)~14.8Ma?
Mobile shale
(H1)~17Ma
SR Shale roller
MP Mud pipe
E1-8 Erosional truncation and/ or unconformity
Intra-fabrics
F1 Basinward-dipping listric faults
C1 Landward-dipping listric faults
Intra reflections

1311 Figure 7

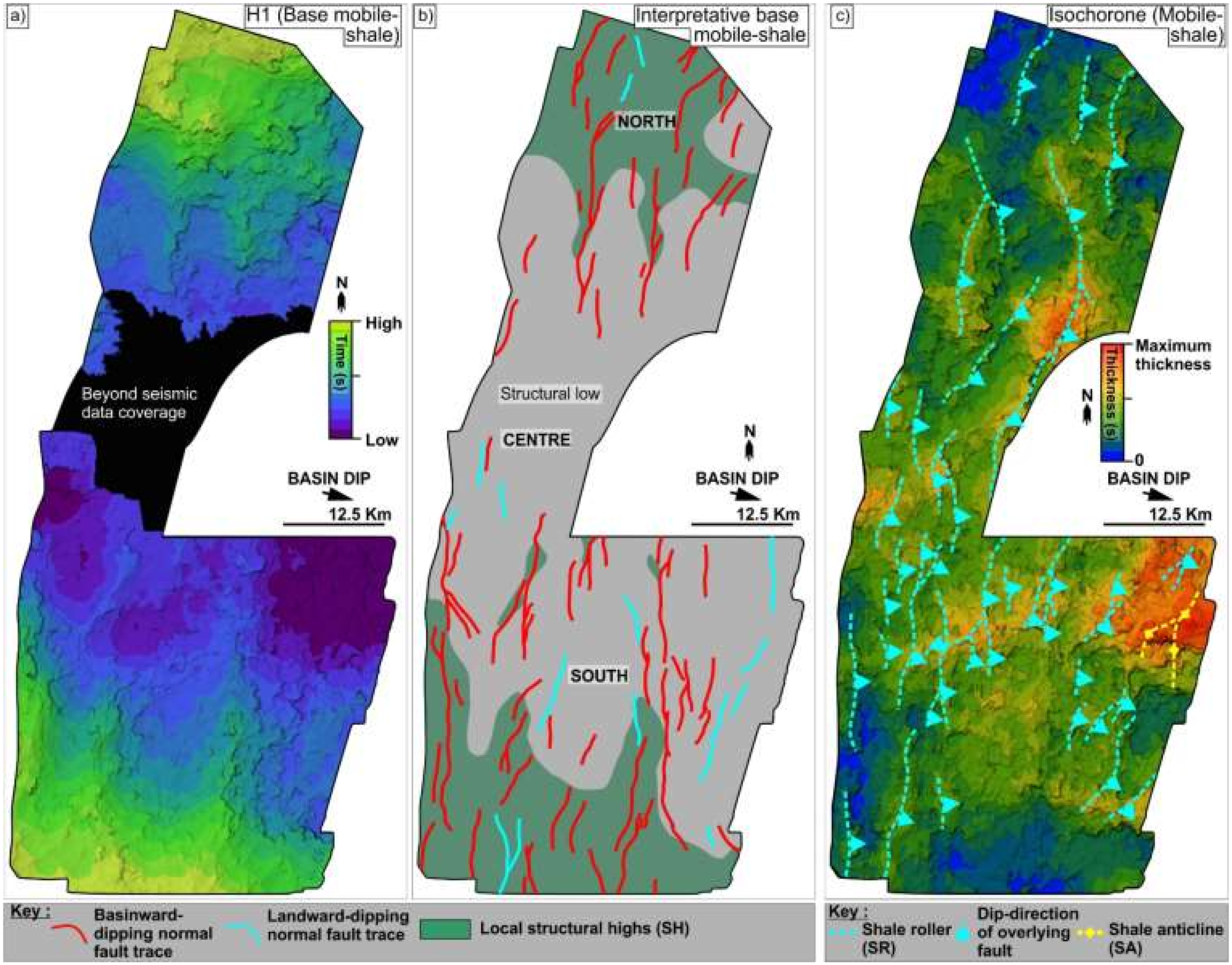

1312

Figure 8

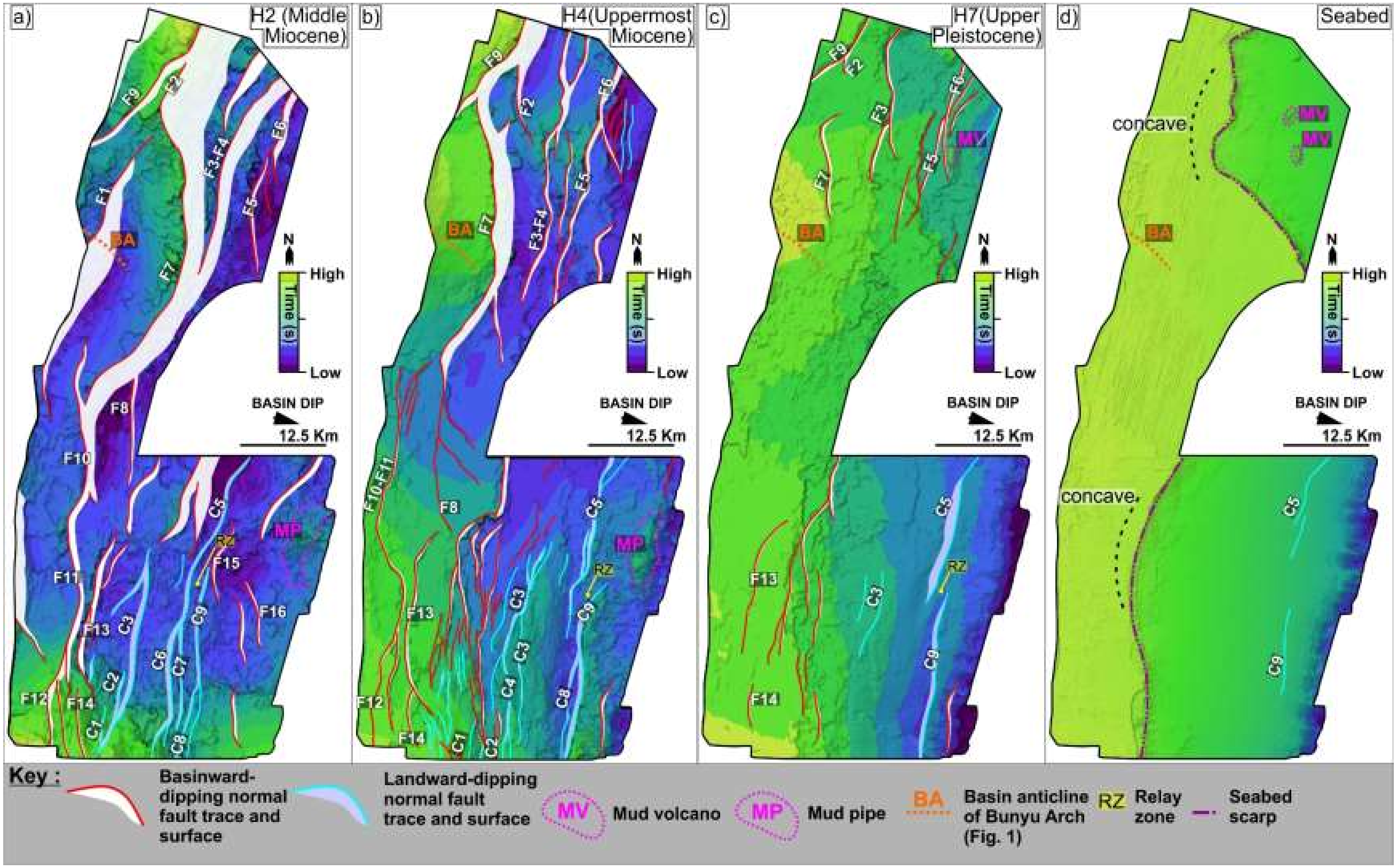

a)
H2 (Middle Miocene)
b)
H4(Uppermost Miocene)
c)
H7(Upper Pleistocene)
d)
Seabed
F1
F2
F3-F4
F5
F6
F7
F8
F9
F10
F11
F10-F11
F12
F13
F14
F15
F16
C1
C2
C3
C4
C5
C6
C7
C8
C9
BA
MP
MV
RZ
concave
N
High
Time (s)
Low
BASIN DIP
12.5 Km
Key :
Basinward-dipping normal fault trace and surface
Landward-dipping normal fault trace and surface
MV Mud volcano
MP Mud pipe
BA Basin anticline of Bunyu Arch (Fig. 1)
RZ Relay zone
Seabed scarp

Figure 9

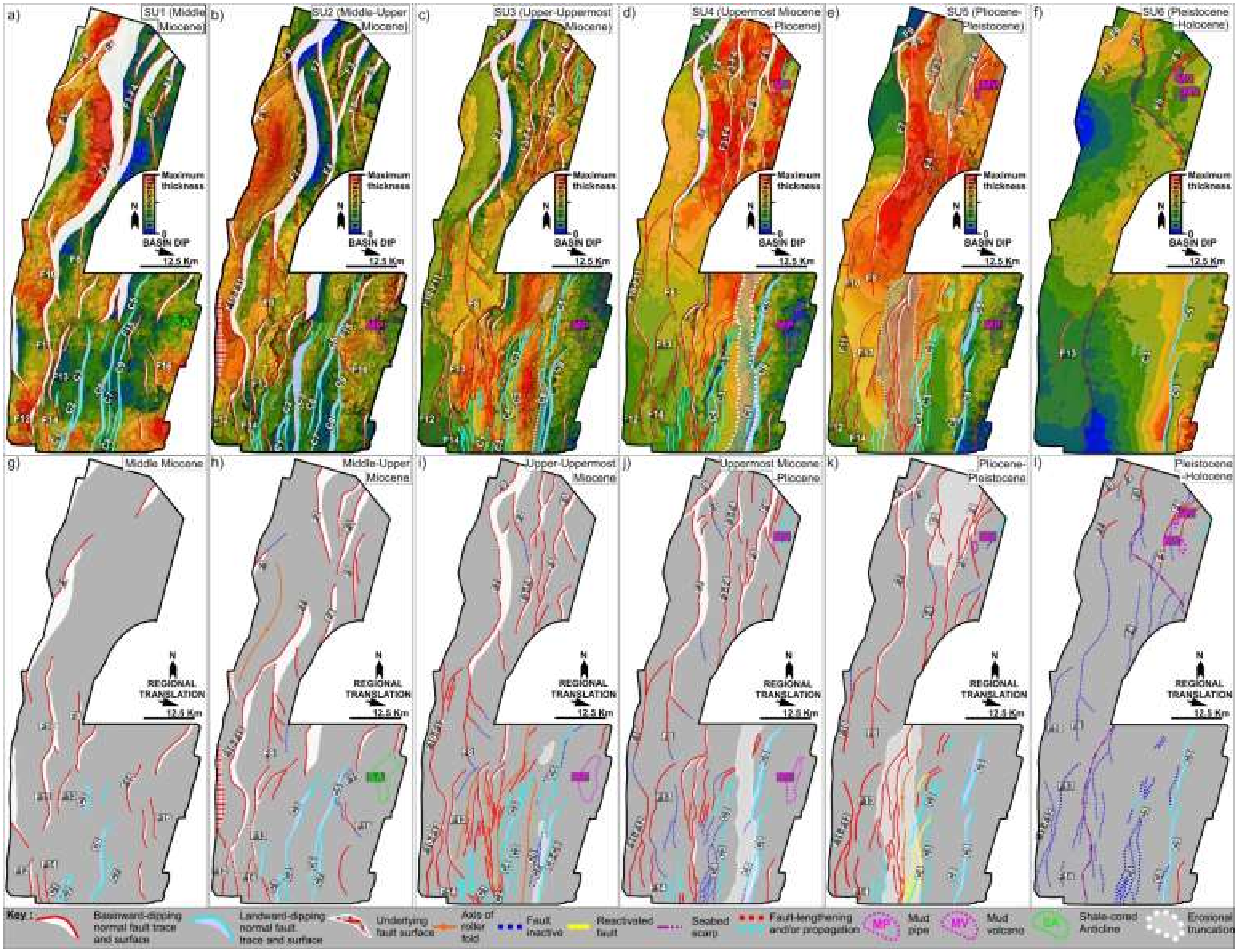
a)
SU1 (Middle Miocene)
b)
SU2 (Middle-Upper Miocene)
c)
SU3 (Upper-Uppermost Miocene)
d)
SU4 (Uppermost Miocene -Pliocene)
e)
SU5 (Pliocene-Pleistocene)
f)
SU6 (Pleistocene -Holocene)
Maximum thickness
0
N
BASIN DIP
12.5 Km
g)
Middle Miocene
h)
Middle-Upper Miocene
i)
Upper-Uppermost Miocene
j)
Uppermost Miocene -Pliocene
k)
Pliocene-Pleistocene
l)
Pleistocene -Holocene
REGIONAL TRANSLATION
Key:
Basinward-dipping normal fault trace and surface
Landward-dipping normal fault trace and surface
Underlying fault surface
Axis of roller fold
Fault inactive
Reactivated fault
Seabed scarp
Fault-lengthening and/or propagation
MP
Mud pipe
MV
Mud volcano
SA
Shale-cored Anticline
Erosional truncation

Figure 10

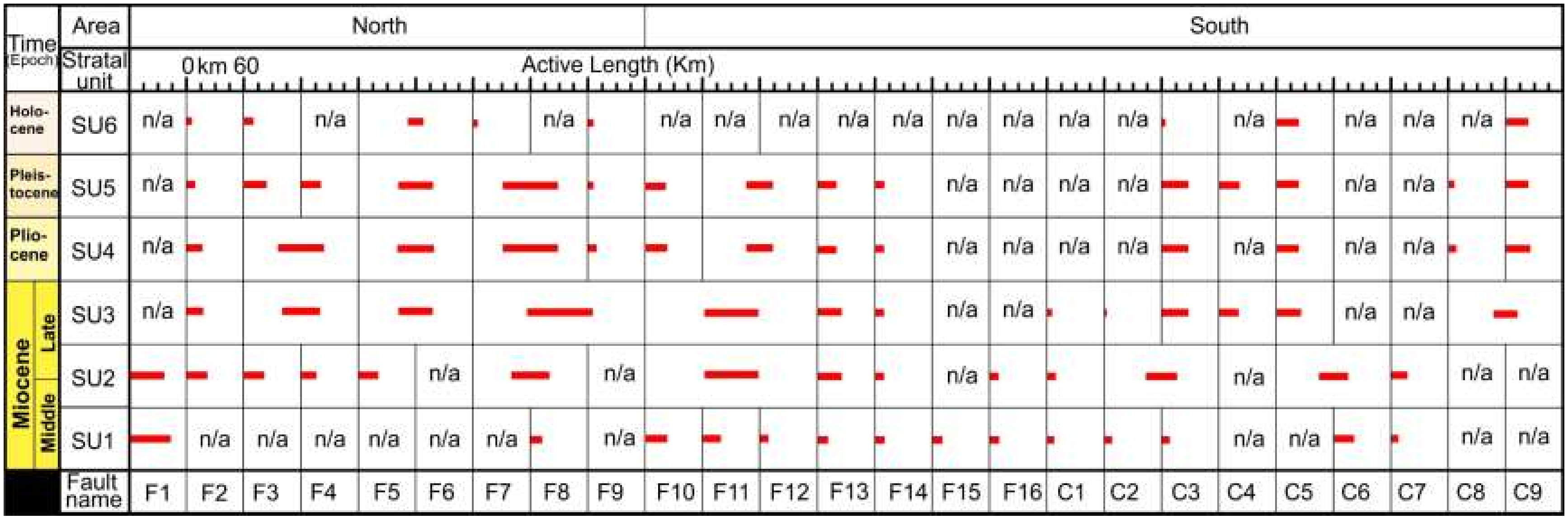
Area
North
South
Time (Epoch)
Stratal unit
0 km 60
Active Length (Km)
Holo-cene
Pleis-tocene
Plio-cene
Miocene
Late
Middle
SU6
SU5
SU4
SU3
SU2
SU1
n/a
Fault name
F1 F2 F3 F4 F5 F6 F7 F8 F9 F10 F11 F12 F13 F14 F15 F16 C1 C2 C3 C4 C5 C6 C7 C8 C9

Figure 11

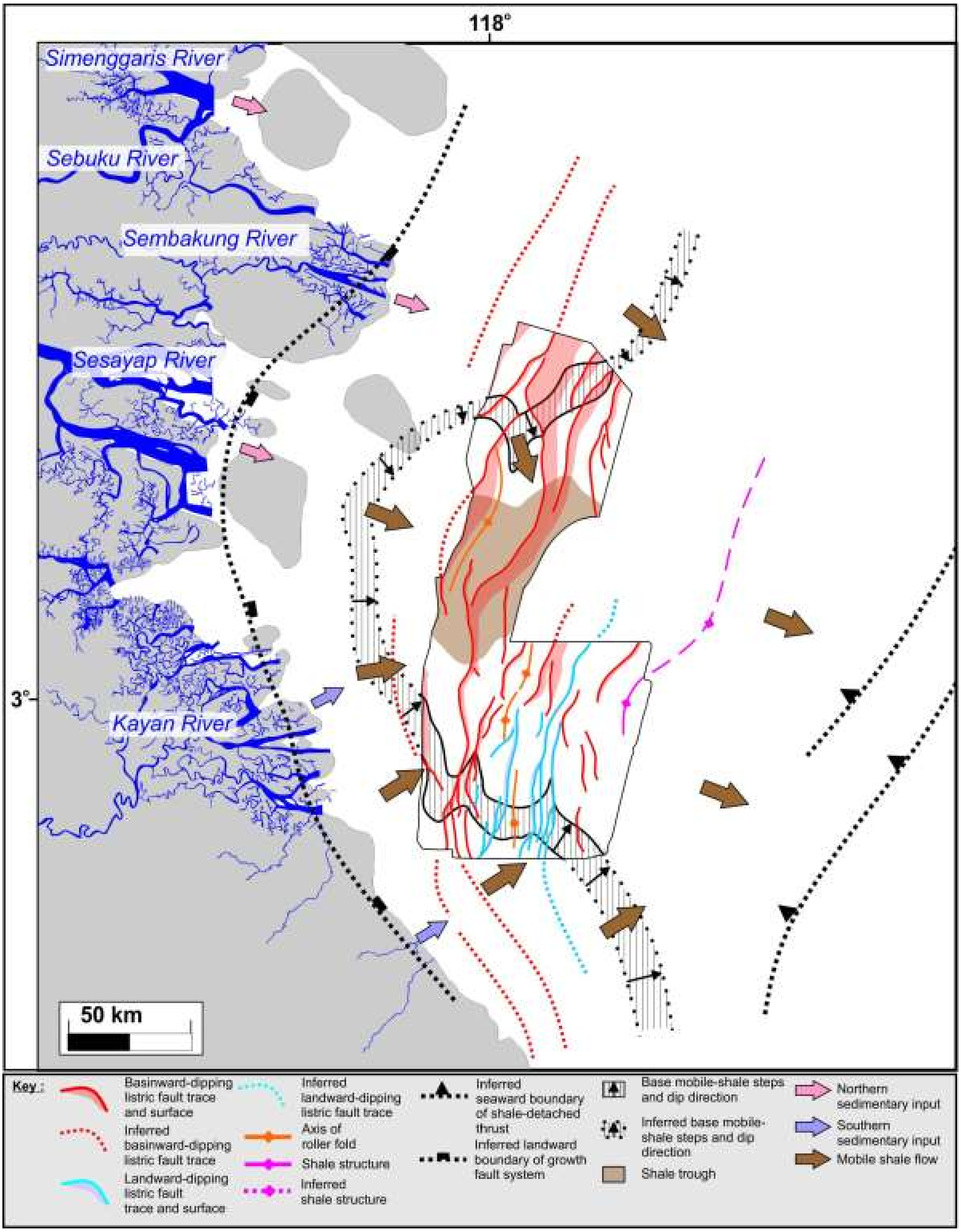

118°
3°
Simenggaris River
Sebuku River
Sembakung River
Sesayap River
Kayan River
50 km
Key :
Basinward-dipping listric fault trace and surface
Inferred basinward-dipping listric fault trace
Landward-dipping listric fault trace and surface
Inferred landward-dipping listric fault trace
Axis of roller fold
Shale structure
Inferred shale structure
Inferred seaward boundary of shale-detached thrust
Inferred landward boundary of growth fault system
Base mobile-shale steps and dip direction
Inferred base mobile-shale steps and dip direction
Shale trough
Northern sedimentary input
Southern sedimentary input
Mobile shale flow